Technical Report Documentation Page

1. Report No.	2. Government Accession No.	3. Recipient's Catalog No.
j.fuel.2025.137433		

4. Title and Subtitle	5. Report Date
Time-resolved spray characterization via unified optical flow and binarization technique	November 2025
	6. Performing Organization Code

7. Author(s)	8. Performing Organization Report No.
O'Brien, C. J., Kang, K., Wood, E. J., Yoon, J., Mayhew, E. K., Kastengren, A., Kweon, C. M., & Lee, T.	

9. Performing Organization Name and Address	10. Work Unit No. (TRAIS)
Center of Excellence for: Alternative Jet Fuels and Environment University of Illinois at Urbana-Champaign, Urbana, IL 61801, USA	11. Contract or Grant No. 13-C-AJFE-UI-051

12. Sponsoring Agency Name and Address	13. Type of Report and Period Covered
Federal Aviation Administration Office of Environment and Energy	Journal Article
	14. Sponsoring Agency Code

15. Supplementary Notes

16. Abstract

This work leverages an unsupervised machine learning and advanced image processing techniques to characterize the breakup of fuel sprays in a small-scale combustor under reacting conditions, providing valuable insights into near-nozzle flow phenomenology. The proposed methodology integrates an improved optical flow model on a convolutional neural network to extract flow vectors with a binarization technique to assess droplets' size and shape across the region of interest. The velocimetry approach demonstrates superior performance compared to a state-of-the-art optical flow model when applied to high-speed X-ray phase contrast spray images, achieving more accurate and reliable flow predictions. Moreover, breakup processes are quantified by breakup length and sphericity in accordance with velocity estimations, allowing a more complete characterization of the flow. This study establishes a robust methodology for analyzing spray morphology and primary breakup in compact combustors, contributing valuable means of understanding and optimizing fuel spray behavior in advanced combustion systems.

17. Key Words	18. Distribution Statement
Liquid combustor, Spray atomization, Image velocimetry, Machine learning, ASCENT	

19. Security Classif. (of this report)	20. Security Classif. (of this page)	21. No. of Pages	22. Price
Unclassified	Unclassified		

Fuel 407 (2026) 137433

Contents lists available at ScienceDirect

Fuel

journal homepage: www.elsevier.com/locate/jfue

Full length article

Time-resolved spray characterization via unified optical flow and binarization technique☆

Casey J. O'Brien[a], Kyungrae Kang[a], Eric J. Wood[a], Joshua Yoon[a], Eric K. Mayhew[c], Alan Kastengren[b], Chol-Bum M. Kweon[c], Tonghun Lee[a,*]

[a] Mechanical Science and Engineering, University of Illinois at Urbana-Champaign, Urbana, IL 61801, USA
[b] X-ray Science Division, Argonne National Laboratory, Lemont, IL 60439, USA
[c] DEVCOM Army Research Laboratory, Aberdeen Proving Ground, MD 21005, USA

HIGHLIGHTS

- Improved unsupervised machine learning enables accurate velocity estimations.
- Spray characteristics for six fuel mass flow rates of a conventional jet fuel are visualized under reacting conditions.
- Time-resolved droplet size, sphericity, velocity, and breakup length are obtained simultaneously.

ARTICLE INFO

Keywords:
Liquid combustor
Spray atomization
Image velocimetry
Machine learning

ABSTRACT

This work leverages an unsupervised machine learning and advanced image processing techniques to characterize the breakup of fuel sprays in a small-scale combustor under reacting conditions, providing valuable insights into near-nozzle flow phenomenology. The proposed methodology integrates an improved optical flow model on a convolutional neural network to extract flow vectors with a binarization technique to assess droplets' size and shape across the region of interest. The velocimetry approach demonstrates superior performance compared to a state-of-the-art optical flow model when applied to high-speed X-ray phase contrast spray images, achieving more accurate and reliable flow predictions. Moreover, breakup processes are quantified by breakup length and sphericity in accordance with velocity estimations, allowing a more complete characterization of the flow. This study establishes a robust methodology for analyzing spray morphology and primary breakup in compact combustors, contributing valuable means of understanding and optimizing fuel spray behavior in advanced combustion systems.

1. Introduction

Fuel spray atomization plays a critical role in the performance and efficiency of combustion systems, including gas turbine engines, diesel engines, and many other propulsion systems. The breakup of bulk liquid fuel into small droplets is essential for maximizing fuel specific surface area, promoting rapid mixing and evaporation [1]. Accelerated breakup processes can improve combustion characteristics significantly. Therefore, many studies have investigated breakup phenomena in various environments and nozzles aiming for enhanced atomization [1–5].

Many phenomenological parameters influence the breakup rate of liquid structures in different ways. For instance, surface tension resists deformation forces and helps retain the liquid structure, but it can also accelerate breakup through capillary pinching by driving the closure of the liquid–gas interface. Among all parameters, velocity is particularly pivotal, governing two key mechanisms of breakup: liquid instability and aerodynamic forces. Near the injector exit, large density gradients between the liquid and the surrounding gas drive Rayleigh–Taylor instabilities. These instabilities lead to the fragmentation of liquid columns and sheets into blobs and ligaments, a process known as primary breakup

☆ Code for this research is available at https://github.com/caseyob22/PC-Flow.

* Corresponding author.
Email address: tonghun@illinois.edu (T. Lee).

https://doi.org/10.1016/j.fuel.2025.137433
Received 16 May 2025; Received in revised form 22 September 2025; Accepted 7 November 2025
Available online 18 November 2025

Nomenclature

Alphabetical

$\mathcal{CV}$	correlation volume
A	projected area
B	batch size
b_m	Bernoulli sampled map
C	channel
F	feature map
H	number of pixels in vertical dimension
I	image
L	loss function
p	pixel
s_k	streamwise location for k % maximum sphericity value
V	velocity
W	number of pixels in horizontal dimension
x	streamwise coordinate
y	transverse coordinate

Greek letters

ν	kinematic viscosity
Ψ	sphericity
ρ	density
σ_x^2, σ_y^2	variance
σ_l	surface tension
σ_{xy}	covariance
τ_b	breakup time
$\theta_1, \theta_2, \theta_t$	spray upper, lower, and total angles

Subscripts and accents

$\hat{X}$	upsampled input
$\widetilde{X}$	warped input
f	final prediction

[6,7]. In this regime, velocity difference at the liquid–gas interface drive shear instabilities, which amplify surface perturbations and contribute to interfacial wave growth and breakup [8].

Once disintegrated into individual blobs and ligaments, aerodynamic forces, competing against surface tension, induce additional breakup. This process is often referred to as secondary breakup [1]. In secondary breakup, although aerodynamic forces dominate, velocity shear can still trigger asymmetric deformations and transverse Rayleigh–Taylor instabilities that promote droplet disintegration in shear-dominated transitional regimes [9]. Moreover, the velocity of the particles can also determine the residence time and turbulence level of evaporated portions, influencing the overall droplet size distribution [10–12], spray dispersion [13,14], and even overall combustion efficiency [15,16]. Therefore, accurate velocity measurement is essential to fully understand and model the breakup dynamics and spray evolution.

Traditionally, there have been refraction, fluorescence, interference, and scattering-based techniques to experimentally characterize sprays with light sources. Shadowgraph and Schlieren imaging are refraction-based techniques where refracted light near the liquid-gas boundary refractive index changes the illumination intensity [17]. Because these methods can accurately capture the multiphase interface, they have been widely used for spray morphology visualization [18]. Scattering-based techniques commonly utilize either Mie or Rayleigh scattering to assess the qualitative size distribution. When combined with fluorescence techniques, these schemes can estimate the Sauter mean diameter (SMD) of the particles on a laser sheet [19]. Also, particle image velocimetry (PIV) using light scattering or fluorescence from the liquid particles is commonly employed to obtain velocity information, although it is often limited for dense sprays [11,19–21]. Alternatively, phase-Doppler particle anemometry (PDPA) can provide both particle velocity and size simultaneously using interferometry of scattered light. However, PDPA is constrained to a point measurement [22,23]. Nevertheless, most conventional techniques face significant challenges in combusting cases as the density gradient, soot incandescence, and soot fluorescence from the combustion can disturb any light sources [24].

Beyond the experimental challenges associated with investigating dense sprays, statistical velocimetry lacks the flexibility required to accommodate a wide range of velocity estimation needs in spray visualization techniques. The complexities of dynamic scenes, characterized by large displacements, occlusions, illumination variations, and the demand for high-resolution predictions at low computational cost, have driven the development of deep learning-based optical flow models. These models enable direct velocity predictions from image pairs, addressing many of the limitations inherent in traditional approaches [25]. Several machine learning models have been developed using both supervised [26–30] and unsupervised [31–36] deep learning approaches. While supervised deep learning models require ground-truth flow fields (labeled datasets) for training, FlowNet [26] was the first to successfully employ convolutional networks for velocity prediction on synthetic datasets. Subsequent developments introduced coarse-to-fine estimation [37], feature warping and cost volumes with deep learning [28], 4-D correlation volumes with recurrent networks [29], and more recently, transformers for full optical flow prediction [30]. This work utilizes an unsupervised learning approach which can be trained without labeled data [38] unlike supervised methods. However, this introduces additional challenges in achieving reliable predictions due to temporal and spatial variations in optical density, particularly occlusion-related issues [32,33,39–41] and alignment issues that require multiple alignment constraints [31,42–47]. Notably, methods such as UFlow [34] and UPFlow [35] have achieved state-of-the-art performance by systematically integrating multiple unsupervised components into a unified framework.

While recent advances in machine learning have improved droplet feature detection [48–50], to the best of the author's knowledge, this work represents the first application of machine learning-based optical flow for spray image velocimetry. Most applications of optical flow in fluid mechanics have been integrated into particle image velocimetry (PIV) using supervised learning approaches [51,52], with additional implementations in bubbly flow analysis [53] and Rayleigh scattering imaging [54]. Although previous efforts elucidated some aspects of multiphase flows, few studies could fully resolve the small-scale nature of atomization. Additionally, experimental techniques usually target a single parameter at a time, potentially conflicting when performing multiple schemes simultaneously. Moreover, most techniques are challenging in combusting environments, failing to reveal spray-combustion interactions. Therefore, this study proposes a unified framework to perform field measurement of critical flow parameters, including velocity, breakup length, size, and shape parameter of the particles in a liquid-fueled combustor under combusting conditions. X-ray phase contrast imaging (PCI) has been employed to minimize disturbances from the density gradient while visualizing droplets in high resolutions and at high repetition rates. An unsupervised machine learning model augmented by an attention mechanism will be introduced to enhance spray feature representations for more accurate flow predictions. Combined with binarization technique, breakup length and particle sphericity analyses will be presented to investigate different breakup behaviors at various flow rates.

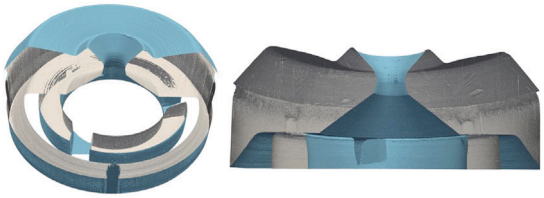

Fig. 1. 3-D reconstruction of the fuel nozzle: (a) isometric view and (b) side view [59].

2. Experimental methods

2.1. ARC-m1 combustor

The ARC-M1 gas turbine combustor was used to perform this study. The combustor was built to represent a single swirl-cup of a midsize gas turbine engine combustor, and it has been used for a variety of previous experiments characterizing lean blow-out (LBO) [55,56], ignition performance [57], and fuel spray breakup behavior [58]. The compact size of the combustor can substantially reduce the fuel consumption needed for characterization.

The ARC-M1 had multiple independently controlled airflow inlet paths, each equipped with an individual mass flow controller and electric resistive heater to create well-characterized inlet conditions. The bulk of the combustor air was introduced through the main air inlet, a portion of which was passed through a radial swirler with an approximate swirl number of 0.6. The dilution air entered through eight dilution ports, introducing air downstream of the fuel nozzle. Additional airflow paths brought air into the combustor along each window to reduce soot formation on the windows, facilitating imaging techniques.

To provide fuel to the combustor, liquid jet fuel was pumped into a piston accumulator and pressurized with nitrogen. A Coriolis liquid mass flow controller (Bronkhorst M14V14I) was used to carefully control the fuel flow rate at the desired value during all testing. The fuel was injected through a hollow-cone pressure-swirl nozzle, which was flush-mounted with the upstream wall to enable full visualization of the spray from the nozzle tip. The internal structure of the tested nozzle was analyzed using X-ray tomography imaging at Argonne National Laboratory's Advanced Photon Source. A 3-D reconstruction of the nozzle, shown in Fig. 1, reveals a converging-diverging outlet section with a minimum and outlet diameter of 344 μm and 882 μm respectively. To start the combustor operation, the fuel-air mixture was ignited using a commercial high-voltage aviation exciter and igniter configuration.

2.2. X-ray phase contrast imaging

High-speed X-ray phase contrast imaging (PCI) was performed on the operating ARC-M1 combustor under stable combusting conditions with a specific focus on the fuel spray immediately after exiting the nozzle. The experiments were performed using the X-ray white beam at Argonne National Laboratory's Advanced Photon Source using beamline 7-BM. The ARC-M1 combustor was equipped with thin X-ray transparent Kapton windows to enable the beam to pass through the combustor. The technique allowed visualization of only the liquid fuel droplets in the combustor, enabled through a combination of X-ray absorption by the fuel and additional diffractions at the boundaries due to the density difference between the fuel and surrounding air [24]. Fig. 2 shows an image of important features of the ARC-M1 combustor as well as the imaging regions measured experimentally. After propagating through the combustor, a 100 μm YAG:Ce scintillator crystal was used to convert some of the incoming X-rays to visible light, which was imaged with a Photron SA-Z high-speed camera fitted with a forward 105 mm f/2.8 lens and a backward 50 mm f/1.2 lens. High-speed images were collected at 90,517 Hz at 640×280 pixels using a camera exposure time of 595 ns. The lens combination provided a resolution of 9.3 μm/pixel, producing an overall imaging region of 5.95×2.60 mm. The first 40 pixels in the horizontal dimension are cropped out in the near-nozzle configuration (600×280 pixels). The setup of the ARC-M1 combustor at Argonne National Laboratory and a schematic summarizing the experimental technique is visualized in Fig. 3.

While the optical flow model developed in this work can be applied to traditional techniques like high-speed shadowgraphy, the quality of the velocity prediction is fundamentally linked to the input image quality. In the dense near-nozzle region of a reacting spray, optical techniques are often limited by signal extinction and beam steering, leading to saturated or poorly resolved image features from which it is difficult to extract reliable motion vectors [19]. X-ray PCI can penetrate the optically dense spray core at high repetition rates and spatial resolution to provide high-fidelity images of the liquid phase. However, this choice represents a trade-off, as the experimental complexity and cost of synchrotron X-ray PCI are significantly higher than for conventional optical setups. Therefore, this technique was specifically chosen to prioritize data quality to resolve the challenging near-nozzle physics that were the focus of this study.

2.3. Dataset

A jet fuel, F-24, was analyzed with six injection fuel flow rates in this study: 26, 30, 35, 37, 40, and 45 g/min. F-24 is a petroleum-derived jet fuel formulated as a drop-in replacement for JP-8, incorporating Jet-A

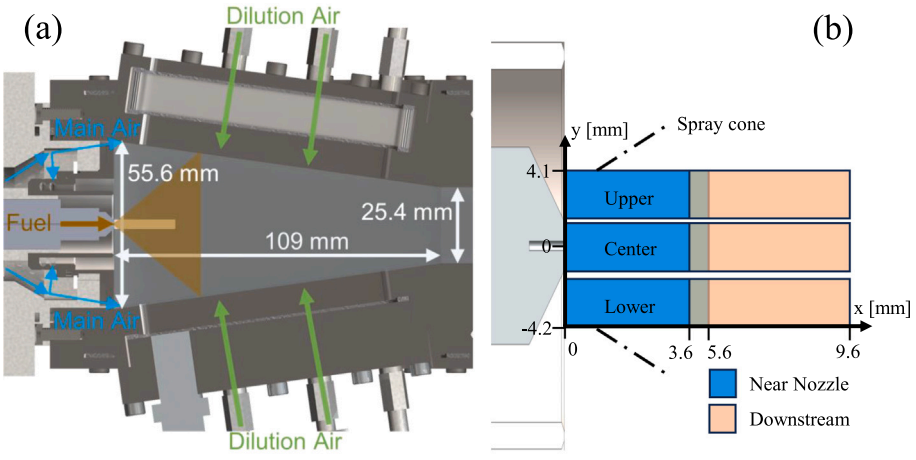

Fig. 2. Schematics of (a) ARC-M1 combustor geometry, and (b) imaging region.

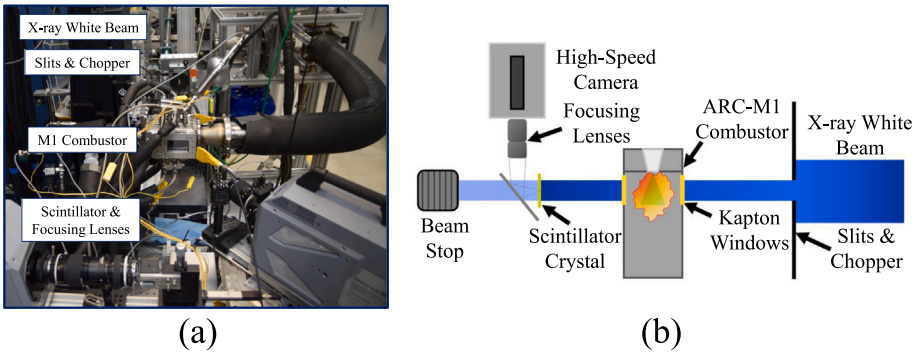

Fig. 3. Experimental setup schematics: (a) test apparatus, and (b) X-ray imaging [59].

Table 1
Physical properties of F-24 at 298 K.

ρ [kg/m^3]	σ_l [mN/m]	ν [mm^2/s]
797	24.8	1.71

with specialized additives. The properties of F-24 fuel are shown in Table 1.

The combustor conditions for the spray measurements were maintained at an inlet air temperature of 323 K and a combustor operating pressure of 1 atm. Two pressure drops across the combustor were tested. For the 26, 30, 35 g/min fuel flow rates, a 1.75 % pressure drop was set, which resulted in 16.1 g/s main and 4.0 g/s dilution air flow rates. For the 37, 40, 45 g/min flow rates, a 3 % pressure drop was set, resulting in 21.3 g/s main and 5.4 g/s dilution air flow rates. The fuel temperature was functionally dependent on the heating of the co-annular main air stream surrounding the nozzle injection, which was approximately 300 K near the injection point for the tested conditions. Measurements were recorded at six imaging regions including center, upper, and lower regions in both near-nozzle and downstream configurations (refer to Fig. 2(b)). The lower and center imaging regions contained 3,792 images each, while the upper region contained 3,773 images. However, data was unavailable for the 26 g/min (lower positions) and 37 g/min (lower and upper positions) flow rates.

2.4. X-ray image preprocessing

While X-ray PCI is a powerful tool for visualizing spray dynamics, the raw images exhibit relatively low contrast due to the marginal X-ray absorption by the liquid fuel, which constitutes only a small fraction of the total incoming X-ray intensity. An example of a raw X-ray image is shown in Fig. 4(a).

To improve the quality of reference images for training optical flow models, a two-step enhancement process was performed. First, a Gaussian blur with a kernel size of 51 was applied to correct for vignetting effects across the dataset. The vignetting pattern was estimated by averaging all input images and applying Gaussian smoothing to model the global intensity variations. A correction mask was then generated by normalizing the estimated vignetting pattern. Each image was subsequently divided by this mask to remove the vignetting effect while preserving the local intensity variations. To eliminate finer-scale and repetitive artifacts such as striations, a mean image was computed across the subset of images and subtracted from each frame. Finally, the images were normalized to ensure a mean intensity value was centered at the median value (128 on an 8-bit integer scale). The results of these preprocessing steps are illustrated in Fig. 4(b).

Following the preprocessing, a self-supervised machine learning denoising algorithm was employed to further enhance the quality of the

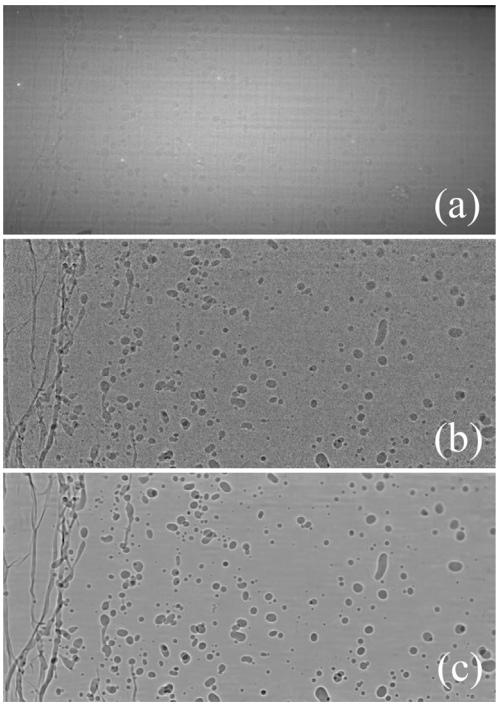

Fig. 4. Preprocessing of X-ray PCI images: (a) raw, (b) Gaussian smoothed and normalized, and (c) denoised.

images in Fig. 4(b). The denoising model used in this work was based on the Self2Self (S2S) framework [60], which enabled single-image blind denoising without requiring clean targets or multiple noisy observations. During training, S2S applied Bernoulli dropout to the input image, where pixels were probabilistically masked. This forced the network to infer missing values from the surrounding context, and the loss was evaluated only over the masked pixels, using the corresponding values from the original noisy image as targets. A similar dropout-based self-supervised denoising strategy was successfully applied to a sequence of X-ray phase contrast images by Oh et al. [61], where clean reconstructions representative of the original distribution were achieved. The denoising architecture adopted in this work followed these established approaches. However, the specifics of the architecture are not the primary focus of this paper, as any method capable of producing high-fidelity images would improve the accuracy of optical flow estimation further down the pipeline.

The denoising algorithm proposed in this study, termed FD-S2S, is outlined in Fig. 5. The method incorporates Bernoulli sampling pixel dropout on the input image with a drop probability of 10 %. Given an

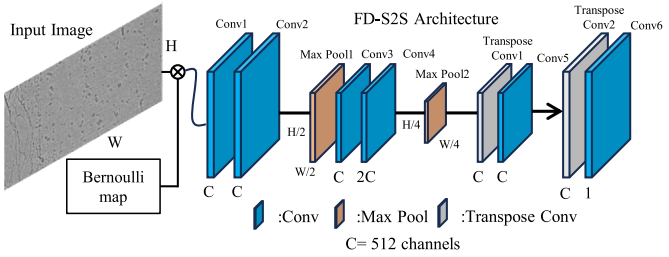

Fig. 5. Schematic of FD-S2S denoising scheme.

input image I, the image is transformed in definition by:

$$I_m := b_m \odot I, \quad \bar{I}_m := (1 - b_m) \odot I. \tag{1}$$

In this equation, I_m is the transformed image with a percentage of masked pixels determined through a Bernoulli distribution. The ground truth, $\bar{I}_m$, corresponds to the original image containing only the target pixels, and the loss function is computed exclusively on these target pixels. Therefore, the loss function can be defined as:

$$\min_{\theta} \left\| \mathcal{F}_{\theta}(I_m) - \bar{I}_m \right\|_{b_m}^2, \tag{2}$$

The model employed an encoder-decoder style architecture using convolutional layers (3×3 kernels, 1×1 final kernel size, stride 1), downsampling via two max pooling layers, and upsampling via transpose convolutions (2×2 kernel size, stride 2). Intermediate layers used ReLU activations and batch normalization, while the final layer used a sigmoid activation and no batch normalization. The training was executed on 3 GeForce RTX 3090 GPUs with AdamW as the optimizer, a global batch size of 6, and a learning rate of 2×10^{-4}. The model was trained over 50 epochs with a learning rate reduction on plateau with a factor of 0.1 and a patience of 5. The training was separated into two cases for the near nozzle and downstream data. An example output from the trained model applied to a preprocessed image is displayed in Fig. 4(c).

The denoising model's performance was quantitatively assessed using multi-scale structural similarity index measure (MS-SSIM) [62], the universal quality image index (UQI) [63], and learned perceptual image patch similarity (LPIPS) with AlexNet [64]. These metrics effectively evaluate image similarity and reconstruction quality, where higher values (approaching 1) indicate better performance for MS-SSIM and UQI, while lower LPIPS values (approaching 0) signify greater perceptual similarity. The current denoising algorithm achieved average scores of 0.88 for MS-SSIM, 0.95 for UQI, and 0.63 for LPIPS, demonstrating its capability to produce high-quality denoised images.

3. Optical flow method

3.1. UPFlow model

The UPFlow model significantly improved unsupervised optical flow performance on public datasets, achieving a 22.2 % improvement on KITTI 2012 [65] and 15.7 % on KITTI 2015 [66]. Two key innovations in UPFlow include a self-guided upsampling module to refine flow predictions and reduce error propagation and a pyramid distillation loss that provides supervision at all prediction stages in the pyramid network. These features addressed issues with fine-scale errors propagating through the model, ensuring more accurate final outputs [35]. UPFlow's low model size and high performance make it an effective baseline for developing a model tailored to spray imaging.

3.2. Proposed optical flow model

The task of predicting velocity vectors that warp the features of an image at time step t to another image at a future time step $t+1$ was formulated via an unsupervised machine learning approach. The proposed

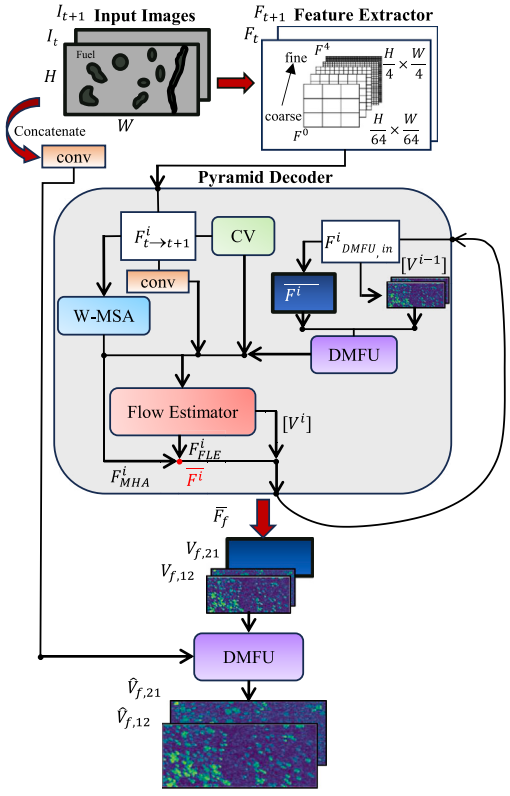

Fig. 6. Architecture of the proposed optical flow estimation.

model was based on UPFlow [35], which employed a coarse-to-fine feature extraction mechanism combined with hierarchical flow estimation. The core of this approach was an encoder-decoder architecture. The encoder extracted hierarchical feature representations using convolutional layers with strided kernels, which remained unchanged in the current study from the UPFlow model. The decoder utilized these feature maps at multiple scales (5 different feature levels) to estimate optical flow iteratively. Specifically, the extracted feature maps at each scale were warped by the previous layer flow estimation, and a correlation volume was obtained between the original and warped features at the relevant prediction time step. At the lowest resolution, no warping was done, and the correlation volume was obtained between the original features. This paper introduces a modified correlation volume and flow estimator that utilized concatenated features from two images to model dependencies between flow directions. Additionally, an attention mechanism was incorporated to enhance feature representations produced by the feature extraction module, while the upsampling module was adapted to learn high-resolution reconstruction through transposed convolutions. The overall architecture of the proposed network is illustrated in Fig. 6.

3.2.1. Correlation volume

The correlation between the warped feature map and the original feature map provides a measure of feature similarity, which is crucial for accurate optical flow estimation. The correlation or cost volume $CV(D, H^i, W^i)$ quantifies the similarity between feature maps at different displacements, where D represents the number of displacement shifts in the second feature map, and H^i, W^i are the spatial dimensions of the input feature map at the ith level. Given an input of the original and warped feature maps at an initial time step, F_t and $\widetilde{F}_t$, the equation for the correlation volume at a displacement d, position (i, j) was computed as:

$$CV(d, i, j) = \sum_{c=1}^{C} \sum_{u,v} F_t^c(i + u, j + v) \cdot \widetilde{F}_t^c(i + u + d_x, j + v + d_y). \tag{3}$$

In Eq. (3), superscript c is the index of the feature channel, d_x and d_y are the displacement offsets in the horizontal and vertical directions, and u and v are the local neighborhood defined by the kernel size of the correlation volume. A kernel size of 1 was used for all test cases, resulting in correlation computations at single-pixel locations without considering a larger local neighborhood. This simplification reduces the above equation to:

$$CV(d,i,j) = \sum_{c=1}^{C} F_t^c(i,j) \cdot \widetilde{F}_t^c(i+d_x, j+d_y). \tag{4}$$

The number of possible displacements, and hence the number of output channels in the correlation volume, depends on the maximum displacement range d_{max}. Given a stride of 1 in both input features, the displacement dimension D is given by:

$$D = (2d_{max}+1)^2 \tag{5}$$

The maximum displacement range was set to 4 pixels (half-width of the window) for consistency with the original UPFlow model. In the baseline approach, two separate correlation computations were performed: one for the forward flow prediction $V_{t\to t+1}$ and another for the backward flow prediction $V_{t+1\to t}$. However, in contrast to the baseline model, the proposed approach computed the correlation volume in a single operation by considering the feature maps and the corresponding warped feature maps for all velocity predictions, which can improve computational efficiency while preserving accuracy. This adjustment incorporated n different combinations of original and warped features, depending on the number of predicted flow fields. The correlation volume was then given by:

$$CV(d,i,j) = \sum_{c=1}^{C}\sum_{n=1}^{N} F_{t_n}^c(i,j) \cdot \widetilde{F}_{t_n}^c(i+d_x, j+d_y). \tag{6}$$

Each channel of the warped input and original feature maps was individually normalized by the mean and standard deviation before computing the correlation volume.

3.2.2. Attention mechanism

A windowed multi-head self-attention mechanism (W-MSA) was applied to the concatenated feature maps extracted from the considered input images. This module refined the feature representations by capturing long-range dependencies across spatial locations while preserving local information. The input to the attention module for each layer i of the pyramid decoder (ranging from 1 to 5) was a tensor F^i_{input} with dimensions $(B, C_{\text{in}}, H^i, W^i)$, where B was the batch size, C_{in} was the number of input feature channels, and H^i, W^i represent the spatial dimensions of the feature maps at layer i. The feature maps were reshaped from (B, C_{in}, H^i, W^i) into an attention compatible feature shape $(B, H^i \times W^i, C_{\text{in}})$. The reshaped input feature was then projected into a lower-dimensional embedding space using a linear transformation. The input was then partitioned into non-overlapping windows. For the first two coarsest layers ($i = 1, 2$), the entire feature map of size (H^i, W^i) was treated as a single window to perform effective global attention. For the subsequent three layers ($i = 3, 4, 5$), the feature maps were partitioned into a grid of square windows, each with a size of $(\frac{W^i}{w^i}, \frac{W^i}{w^i})$, where w^i was a divisor from the set $\{2, 4, 8\}$, respectively. Zero padding was used to ensure divisibility in feature map. This was followed by layer normalization to stabilize training. This resulted in an embedding feature map denoted as F_{embed} with shape $(B \times N_{windows}, L^i, C_{\text{in}})$, where $L^i = H^i \times W^i$ for the two coarsest layers and $L^i = (\frac{W^i}{w^i})^2$ for the windowed layers.

Multi-head self-attention computation. The attention operation followed the standard scaled dot-product attention formulation [67]:

$$\text{Attention}(\mathcal{Q}, \mathcal{K}, \mathcal{V}) = \text{softmax}\left(\frac{\mathcal{Q}\mathcal{K}^T}{\sqrt{d_k}}\right)\mathcal{V}, \tag{7}$$

where $\mathcal{Q}$, $\mathcal{K}$, and $\mathcal{V}$ are the query, key, and value matrices, respectively, and d_k is the key vector dimension. A multi-head formulation with four attention heads was utilized to attend to unique windowed representations, and positional encoding was not implemented. The self-attended features were enhanced by incorporating a residual connection with the pre-layer normalized features ($F_{\text{embed, PLN}}$):

$$F_{\text{attended}} = F_{\text{embed, PLN}} + \text{Attention}(F_{\text{embed}}), \tag{8}$$

where the residual connection ensures that the refined features retain information from the original input. The attended features were then projected to the desired output dimension C_{out} via an additional linear layer. The output features from the linear layer, F^i_{out}, were subsequently reshaped back to the original spatial structure (B, C_{out}, H^i, W^i). This transformation enabled the enhanced feature maps to remain compatible with subsequent layers of the model for integration into the learning pipeline.

3.2.3. Pyramid flow estimation

The prediction of flow vectors at each pyramid level was performed using a densely connected multi-layer convolutional neural network (CNN) with a layer architecture identical to the UPFlow model. This dense multi-layer CNN shared weights between all levels of the pyramid prediction. The network consisted of five convolutional layers, with a fixed number of feature channels set to 128, 128, 96, 64, and 32 across all levels. In the UPFlow model, the flow estimator architecture processed each flow prediction ($V_{t\to t+1}$ and $V_{t+1\to t}$) individually, but the weights were shared across these predictions. The inputs to the flow estimator in the UPFlow model included the cost volume, the feature map, and the upsampled optical flow of the target velocity prediction, and the output was the individual flow prediction ($V_{t\to t+1}$ or $V_{t+1\to t}$) at the ith level.

In contrast, the proposed approach modified the flow estimator's inputs by incorporating a combined correlation volume, feature maps of all input images transformed through a 1×1 convolution, all upsampled optical flow predictions considered, and attention transformed features. By leveraging this expanded feature set, the flow predictor estimated all flow outputs at the current scale simultaneously, corresponding to the ith level. Additionally, unlike the original UPFlow model, the proposed approach did not utilize a context network with dilated convolutions.

3.2.4. Upsampler

A key contribution of the UPFlow model was the learned self-guided upsampling module, which refined optical flow predictions using an interpolation flow U^i and an interpolation mask B^i. This module improved upon standard bilinear upsampling by blending the bilinear upsampled flow with a warped version of the same flow using the interpolation flow. The interpolation mask determined the weighting between these two components. This upsampling process ensured that the optical flow predictions aligned with the feature map resolutions at each successive pyramid level.

The proposed model employed a shared convolutional upsampling architecture that increased the resolution of flow predictions by a factor of 2, maintaining alignment with the feature maps in the next pyramid level. Dense block connections were utilized for all convolution and transpose convolution layers. All learned upsampling was achieved through a transpose convolution operation with a kernel size of 2×2 and a stride of 2. Unlike UPFlow, which used bilinearly upsampled features as inputs, the proposed model directly processed the lower-resolution features from the previous level $i-1$. Specifically, the inputs to the proposed upsampling module consisted of (1) concatenated flow predictions, (2) input features to the final convolutional layer in the flow estimator that were transformed by a 1×1 convolution to reduce the channel dimension to 32, denoted as F^i_{FLE}, and (3) attended pyramid features from the previous level. An overview of the proposed upsampling module, referred to as the Dual-Mode Flow Upsampler (DMFU), is shown in Fig. 7. Leaky ReLU activations with a negative slope of

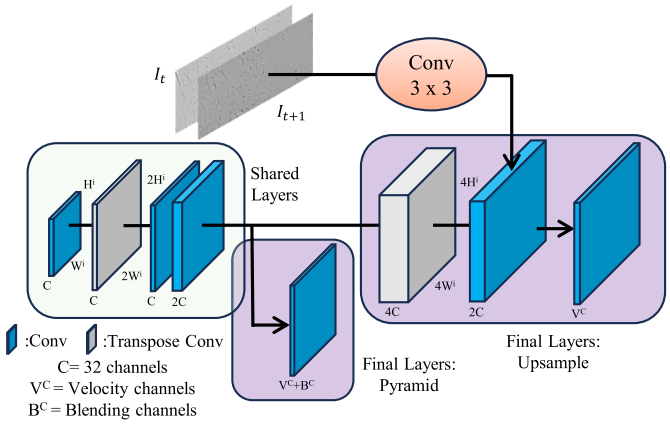

Fig. 7. Overview of the upsampling module.

0.1 were applied after all layers except the final output layer. Unlike methods that compute forward and backward flows independently, the proposed model predicted all flows at each level simultaneously within a single execution of the upsampling module.

Pyramid computation. During the pyramid refinement process, an interpolation-based upsampling strategy was employed. The upsampled velocity prediction at level i, denoted as $\hat{V}^{i-1}$, was computed using a weighted combination of a network-predicted upsampled flow and a bilinear upsampled flow. The interpolation mask B^i controlled this blending process with element-wise multiplication $\odot$:

$$\hat{V}^{i-1} = B^i \odot U^i + (1 - B^i) \odot V_{\text{bilinear}}, \tag{9}$$

where U^i represents the upsampled flow predicted by the DMFU block, and V_{bilinear} is the bilinear upsampled flow from the previous level. The interpolation mask B^i, generated in the DMFU block by a sigmoid activation function, acted as a confidence map, determining the extent to which the refined optical flow should be weighted against the bilinear upsampling method. The interpolation mask had a single output channel for a given flow prediction, which corresponded to the confidence weighting applied to both velocity components, V_x and V_y. Warping was not applied in this final determination of $\hat{V}^{i-1}$.

Final upsampling. After the completion of the pyramid refinement process, the optical flow predictions, attended features, and layer outputs F_{FLE} reach a spatial resolution of $H/4 \times W/4$. To obtain the final high-resolution optical flow, the DMFU processed the input features through shared layers, followed by distinct final layers that upsampled the output by an additional factor of 2. Additionally, the final output channels differed from the pyramid computation. Instead of relying on the interpolation-based blending mechanism, the model directly predicted $\hat{V}_f$ as the final optical flow estimate. This direct upsampling approach eliminated the interpolation mask and produced the final optical flow without blending with a bilinear upsampled counterpart. To further enhance the final flow estimation, concatenated raw input images were processed through a single 3×3 convolutional layer, and the resulting features were injected into the first convolutional layer of the final stage. This step ensured that the model retained fine spatial structures and less abstract features from the original images, complementing the learned representations from preceding layers and improving the accuracy of the final optical flow prediction.

3.2.5. Unsupervised optical flow loss

The primary objective of the proposed unsupervised optical flow model was to minimize discrepancies between consecutive image frames while enforcing motion smoothness and constraining overshooting velocity predictions. Instead of utilizing traditional photometric losses rooted in strict brightness constancy, the model incorporated structural similarity (SSIM) loss, which provided greater robustness against illumination and structure variations. While photometric losses are not universally generalizable across datasets, SSIM yielded the best results on the X-ray PCI dataset when combined with other unsupervised losses. Furthermore, an ablation study on publicly available datasets demonstrated that SSIM is competitive with census loss in unsupervised optical flow estimation [34].

To further regularize motion estimates, a background motion penalty was introduced that suppressed excessive velocity predictions in non-moving regions. This background loss term was not included in the UPFlow model for future comparisons, as it led to training instability and model divergence. Occlusion handling was not explicitly considered in the loss formulation, as the X-ray PCI dataset did not contain meaningful occlusions. Overlapping fuel structures in the dataset appeared as darker pixel regions due to correlated intensity variations, and the dynamic range was typically not fully saturated. The only significant occlusions arose when fuel structures moved out of the image frame, which affected only a small fraction of the predicted flow distribution.

SSIM loss. To ensure structural consistency between consecutive frames, the unweighted SSIM loss was defined as:

$$L_{\text{SSIM}} = \frac{1}{N_w} \sum_p \left(\frac{1 - \text{SSIM}(I_{t+1}(p), I_t(p + \hat{V}_f(p)))}{2} \right), \tag{10}$$

where SSIM computed the local structural similarity between the warped next frame $\tilde{I}_{t+1}$ and the reference frame I_{t+1}, and N_w is the number of windows. The SSIM function was computed using a 3×3 average pooling operation and was defined as a combination of the contrast and structural terms, excluding the luminance term:

$$\text{SSIM}(I_x, I_y) = \frac{(2\sigma_{xy} + c_1)}{(\sigma_x^2 + \sigma_y^2 + c_1)}, \tag{11}$$

where a regularization constant c_1 was included to avoid numerical instability.

Background loss. To prevent motion estimates in non-moving regions, a background loss was implemented using a low-order norm:

$$L_{\text{bg}} = \frac{1}{N_p} \sum_p \left(\sqrt{V_x(p)^2 + V_y(p)^2} \right)^{0.2}, \tag{12}$$

where V_x, V_y represent the horizontal and vertical components of the predicted flow. N_p is the number of pixels. The exponent 0.2 attenuates the influence of large velocity magnitudes in the loss function while still discouraging non-zero motion in background regions.

Final loss function. In addition to the SSIM and background losses, additional unsupervised regularization terms commonly used in optical flow estimation were incorporated. These included a census loss L_c [39], a second-order edge-aware smoothness loss L_s [32], and the pyramid distillation loss L_d developed in the UPFlow model [35]. The final loss function was expressed as:

$$L = L_{\text{SSIM}} + \lambda_{\text{bg}} L_{\text{bg}} + \lambda_{\text{c}} L_{\text{c}} + \lambda_{\text{s}} L_{\text{s}} + \lambda_{\text{d}} L_{\text{d}}, \tag{13}$$

where λ_{bg}, λ_{c}, λ_{s}, and λ_{d} were hyperparameters set to $\lambda_{\text{bg}} = 0.125$, $\lambda_{\text{c}} = 1.0$, $\lambda_{\text{s}} = 0.05$, and $\lambda_{\text{d}} = 0.02$.

3.2.6. Training settings

Two separate training cases were conducted on the near-nozzle and downstream X-ray PCI images, each consisting of 30,279 images for combined 26, 30 and 35 g/min fuel flow rate conditions. The method was implemented in PyTorch using the Adam optimizer. The UPFlow model was trained with a batch size of 4, consistent with its original training

Table 2
Architectural comparison of different model configurations.

Model	Attention	Parameters	Train Time [s/iteration]
UPFlow		3.49 M	0.109
PC-Flow NA		2.85 M	0.092
PC-Flow	✓	3.11 M	0.091

Table 3
Performance comparison of different model configurations.

Model	MAE [A.U.][1]	LPIPS	MS-SSIM	PSNR [dB]
UPFlow	3.19	0.053	0.96	33.25
PC-Flow NA	2.49	0.038	0.98	35.51
PC-Flow	2.36	0.034	0.98	36.19

[1] A.U. denotes "arbitrary unit".

procedure, and a learning rate of 2×10^{-4} provided the best results, as higher values lead to divergence. For the proposed models, a batch size of 6 was used with a learning rate of 1×10^{-3}. Training was conducted over 60 epochs on GeForce RTX 3090 GPUs.

Comparative evaluations were performed using only the near-nozzle dataset, as this dataset exhibited more irregular flow structures and vigorous breakup, leading to higher prediction errors. This dataset was more difficult to model accurately, so it served as a suitable benchmark for comparison. Three different model architectures were trained. These included the original UPFlow model, the proposed new model architecture without the attention mechanism (PC-Flow NA), and the same architecture with the attention mechanism (PC-Flow). The attention mechanism introduced approximately 0.26 million additional parameters in the baseline proposed flow prediction approach.

Table 2 summarizes each model's configuration, parameter size, and training time. Training time is reported per image pair sequence. The performance of each model was evaluated using four measures, including mean absolute pixel intensity error (MAE) in arbitrary units on an 8-bit integer scale, multi-scale structural similarity index measure (MS-SSIM), learned perceptual image patch similarity (LPIPS), and peak signal-to-noise ratio (PSNR), to assess how well the predicted flow warped the initial image I_t to match the reference future image at I_{t+1}.

The trained PC-Flow model on the low-flow conditions ($\{26, 30, 35\}$ g/min) was then applied during inference to the high-flow conditions ($\{37, 40, 45\}$ g/min) at the respective imaging region. For the high-flow set, ten pixels were cropped from the top and bottom of the center imaging position before inference to remove artifacts at the image edges. The high-flow conditions were not utilized in model comparisons (Sections 3.2.7 and 3.2.8).

3.2.7. Performance comparison of models

To assess the overall performance of different models, the MAE, LPIPS, MS-SSIM, and PSNR were analyzed, averaged over the entire near-nozzle dataset for a single time-step comparison. The results of this evaluation are presented in Table 3.

Lower values signify better results for MAE and LPIPS, whereas higher values for MS-SSIM and PSNR. The proposed models achieved increased performance across all tested cases. The addition of an attention mechanism further improved accuracy, reducing error in the proposed model by 5.4 % in terms of MAE, reinforcing its role in refining flow estimation. In particular, PC-Flow reduced MAE by 29.9 % compared to the UPFlow model, showing its effectiveness in improving flow predictions.

Beyond single-step predictions, this evaluation was extended to analyze error propagation over increasing temporal steps, specifically up to $t+5$. This process involved warping an initial image forward in time using precomputed flows, continuously propagating the initial image pixel information to future frames. The warped image was compared at each step to the corresponding reference frame to compute error metrics. The results of this temporal evaluation are shown in Fig. 8, averaged over the entire near-nozzle dataset.

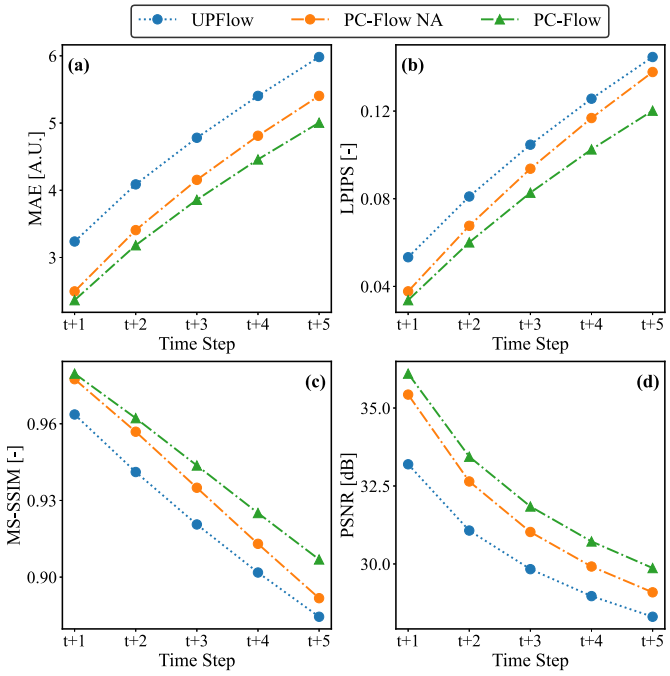

Fig. 8. Error propagation analysis for different models: (a) MAE, (b) LPIPS, (c) MS-SSIM, and (d) PSNR.

While the proposed models yielded lower errors across the temporal evaluation, the PC-Flow model specifically showed a more favorable error propagation with a flatter gradient compared to the PC-Flow NA model. This characteristic can be indicative of improved generalization of spray features and reduced overfitting.

To quantitatively assess this generalization, the PC-Flow model trained solely on the near-nozzle data was tested on the downstream dataset. This cross-domain inference yielded MAE, LPIPS, MS-SSIM, and PSNR values of 2.98, 0.028, 0.97, and 34.12, respectively. The same PC-Flow architecture trained and tested directly on the downstream data achieved metrics of 2.91, 0.027, 0.98, and 34.34.

3.2.8. Detailed comparison: PC-flow vs. UPFlow

After establishing the average comparative model performance trends, the analysis focuses on the best-performing model PC-Flow in comparison to UPFlow. This subsection presents a detailed evaluation across all imaging positions and fuel flow rates. Table 4 summarizes the results across upper, lower, and center regions for multiple fuel flow rates.

The PC-Flow model showed lower errors and higher accuracy than UPFlow under all conditions, demonstrating superior performance in preserving critical flow structures. The improvement remained consistent, with an approximate 30 % reduction in MAE across all flow rates and regions. The high MS-SSIM values (close to 1) and low LPIPS scores (near 0) across all test conditions indicate that PC-Flow effectively reconstructed relevant structures in future images through warping, providing confidence in the current model's ability to generate accurate flow predictions.

Beyond quantitative metrics, it was also essential to evaluate the qualitative agreement of the predicted flow structures, as ground truth flow data was unavailable. As shown in Fig. 9, PC-Flow's predictions remained well-localized to fuel structures, exhibiting minimal background motion. In contrast, UPFlow produced noisier predictions, where distinguishing fuel structures becomes challenging.

One potential strategy to mitigate UPFlow's background noise is to apply binarization techniques to isolate structures of importance. However, this approach introduces uncertainty, as background noise

Table 4
Comparison of PC-Flow and UPFlow in different imaging regions.

Model	Flow Rate [g/min]	MAE [A.U.][1]	LPIPS	MS-SSIM	PSNR [dB]
PC-Flow					
	Upper:				
	26.0	1.85	0.027	0.99	38.27
	30.0	1.95	0.030	0.98	37.75
	35.0	2.19	0.037	0.98	36.62
	Lower:				
	30.0	1.94	0.029	0.98	37.78
	35.0	2.08	0.034	0.98	37.03
	Center:				
	26.0	2.77	0.033	0.98	34.63
	30.0	2.91	0.036	0.97	34.21
	35.0	3.22	0.043	0.97	33.24
UPFlow					
	Upper:				
	26.0	2.48	0.042	0.97	35.33
	30.0	2.61	0.047	0.97	34.88
	35.0	2.91	0.056	0.97	33.97
	Lower:				
	30.0	2.58	0.047	0.97	34.83
	35.0	2.71	0.053	0.97	34.35
	Center:				
	26.0	3.84	0.053	0.96	31.43
	30.0	4.01	0.059	0.95	31.04
	35.0	4.39	0.069	0.95	30.19

A.U. denotes "arbitrary unit".

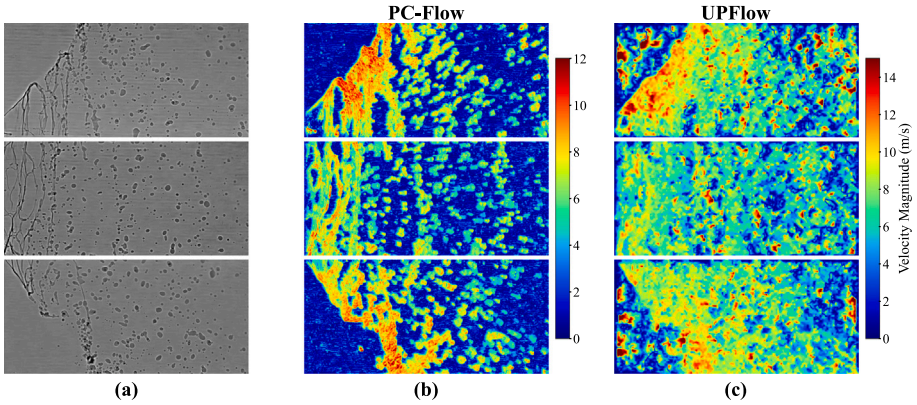

Fig. 9. An example comparison of flow predictions: (a) raw images, (b) PC-Flow, and (c) UPFlow.

may become entangled with the foreground in the warping process, leading to unrealistic and unreliable results. The enhanced localization in the PC-Flow model provides greater confidence in the physical accuracy of the flow prediction and can potentially reduce the need for additional statistical binarization techniques. Exploring optical flow as a direct structure localization method remains a promising direction for future research, offering a pathway to more robust fuel structure identification without dependence on post-processing techniques.

3.3. Binarization

To extract meaningful regions from the grayscale image, an adaptive thresholding-based binarization approach was implemented, followed by morphological operations for refinement. A visualization of the binarization technique applied to a stack of input images is presented in Fig. 10.

First, adaptive mean thresholding was applied, which dynamically determined the threshold for each pixel based on the mean intensity of its local neighborhood. This method helped account for varying illumination conditions across the image. After thresholding, a morphological dilation operation was applied using a 4×4 rectangular structuring element. This step expanded the segmented regions, helping close small gaps and connect fragmented structures. Next, an erosion operation was employed with a 3×3 structuring element to refine the segmentation by removing small artifacts while preserving the spray structures. Finally, a closing operation was performed, which consisted of a dilation followed by an erosion using a 4×4 rectangular structuring element. The resulting binary masks were then used for further analysis. The choice of morphological operations is inherently experimental but can be used to align features to human perception [68–70]. An initial small net dilational effect was chosen to prioritize the connectivity of the fuel sheet structure. Concurrently, small kernel sizes were utilized to minimize alterations to the original binarization structure.

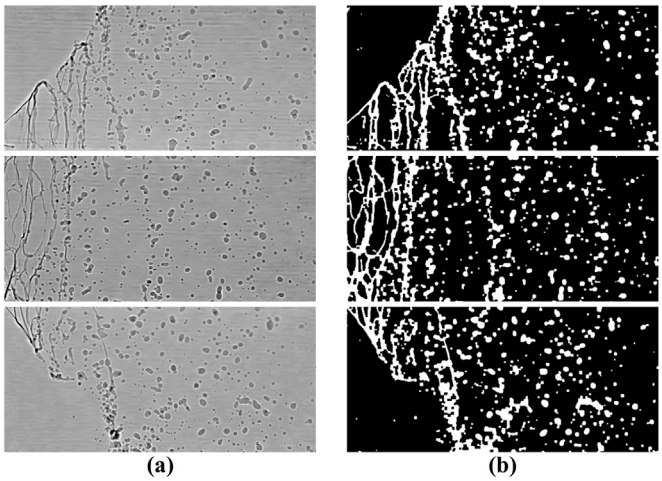

Fig. 10. Sample binarized images: (a) raw and (b) binarized.

3.4. Uncertainty quantification for the PC-flow model

In the traditional sense, optical flow relies on three fundamental assumptions of brightness constancy, smooth motion, and small displacements [71,72]. Brightness constancy, an individual pixel's intensity value remains constant as it moves from one frame to another, is expressed as:

$$I(x, y, t) = I(x + V_x, y + V_y, t + 1). \tag{14}$$

This equation can be linearized under the assumption of small displacements as [73]:

$$\frac{\partial I}{\partial x}V_x + \frac{\partial I}{\partial y}V_y + \frac{\partial I}{\partial t} = 0, \tag{15}$$

leading to the development of iterative coarse-to-fine techniques for flow estimation. However, Eq. (15) results in an ill-posed problem with two unknowns u and v from a single equation, also known as the aperture problem [25]. The early leading formulations to constrain this equation relied on a global smoothness constraint in the Horn-Schunck method [74] and a local smoothness constraint in the Lucas-Kanade methodology [75]. Although many modern methods are based on Horn-Schunck principles, its global smoothing can lead to over-smoothing of flow boundaries and small scale features [76]. Lucas-Kanade's local approach is arguably more effective for quantifying the uncertainty of specific, local features such as droplets.

The Lucas-Kanade methodology addresses the optical flow problem by using a window solution, which generates an over-determined system of linear equations for each pixel within a given window $\mathcal{W}$. This system is solved using a least squares solution derived from a Taylor expansion.

$$v = (A^T A)^{-1} A^T b, \tag{16}$$

where:

$$A = \begin{bmatrix} \frac{\partial I}{\partial x}(\mathcal{W}_1) & \frac{\partial I}{\partial y}(\mathcal{W}_1) \\ \frac{\partial I}{\partial x}(\mathcal{W}_2) & \frac{\partial I}{\partial y}(\mathcal{W}_2) \\ \vdots & \vdots \\ \frac{\partial I}{\partial x}(\mathcal{W}_n) & \frac{\partial I}{\partial y}(\mathcal{W}_n) \end{bmatrix}, v = \begin{bmatrix} V_x \\ V_y \end{bmatrix}, b = \begin{bmatrix} -\frac{\partial I}{\partial t}(\mathcal{W}_1) \\ -\frac{\partial I}{\partial t}(\mathcal{W}_2) \\ \vdots \\ -\frac{\partial I}{\partial t}(\mathcal{W}_n) \end{bmatrix} \tag{17}$$

The uncertainty in the optical flow vector is fundamentally tied to the structure matrix M that defines the ambiguity of the features in the target image ($A^T A$) as also written in [77,78]:

$$M = \begin{bmatrix} \sum (\frac{\partial I}{\partial x})^2 & \sum \frac{\partial I}{\partial x}\frac{\partial I}{\partial y} \\ \sum \frac{\partial I}{\partial x}\frac{\partial I}{\partial y} & \sum (\frac{\partial I}{\partial y})^2 \end{bmatrix}, \tag{18}$$

and the unbiased estimation of the noise variance σ_n^2:

$$\sigma_n^2(p) = \frac{\sum_{p\in\mathcal{W}} (\epsilon(p) - \bar{\epsilon})^2}{N - 2}. \tag{19}$$

The sample variance, $\sigma_n^2(p)$, was calculated over an $n \times n$ window of $N = n^2$ pixels. This variance was derived from the residual $\epsilon(p)$, which was the photometric difference between the warped image, $\widetilde{I}(p)$, and the reference image, $I(p)$.

$$\epsilon(p) = \widetilde{I}(p) - I(p). \tag{20}$$

Therefore, the velocity prediction covariance was estimated at pixel p, with an added regularization constant ($c_1 = 10^{-8}$) to diagonal of M:

$$Cov(v(p)) = (M + c_1 \boldsymbol{I})^{-1}(p) \cdot \sigma_n^2(p). \tag{21}$$

The uncertainty framework, which approximated the aleatoric uncertainty of the PC-Flow model's predictions, had limitations. Specifically, it provided minimal insight into the model's epistemic uncertainty. To address this, future research could pose the model architecture in a probabilistic framework for flow predictions [79]. In this study, a 3×3 window was used to calculate the noise variance and the structure matrix. The small window size aligned with the local smoothness assumption of the Lucas-Kanade methodology, even though the PC-Flow model had an effectively larger field-of-view through coarse-to-fine estimation. A larger window size would reduce the singularity of the structure matrix and decrease the velocity variance. The per-pixel variance was used to determine the average per-pixel standard uncertainty of the velocity magnitude in binarized regions through error propagation:

$$\sigma_{||\vec{v}||} = \sqrt{\left(\frac{V_x}{||\vec{v}||}\right)^2 \sigma_{V_x}^2 + \left(\frac{V_y}{||\vec{v}||}\right)^2 \sigma_{V_y}^2 + 2\left(\frac{V_x}{||\vec{v}||}\right)\left(\frac{V_y}{||\vec{v}||}\right)\sigma_{V_{xy}}}. \tag{22}$$

The per-pixel average uncertainty of the velocity magnitude for binarized regions is presented in Fig. 11. The uncertainty was visibly highest near the frame boundaries and along the edges of the spray sheet. It is conjectured that the uncertainty was higher at spray cone edges because of high optical complexity and rapid feature changes. Similarly, the lack of data and features at spray and frame boundaries contributed to higher uncertainty. A broader view of the uncertainty is provided in Fig. 12, which displays the average uncertainty per velocity component for binarized regions throughout the time sequence and for each imaging position. Overall, average sub-pixel certainty (1 pixel/frame = 0.84 m/s) was achieved for both velocity components under all flow conditions.

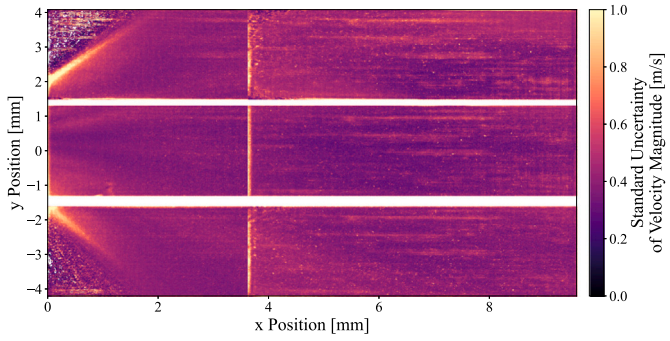

Fig. 11. Average per-pixel uncertainty of velocity magnitude at a fuel flow rate of 35 g/min.

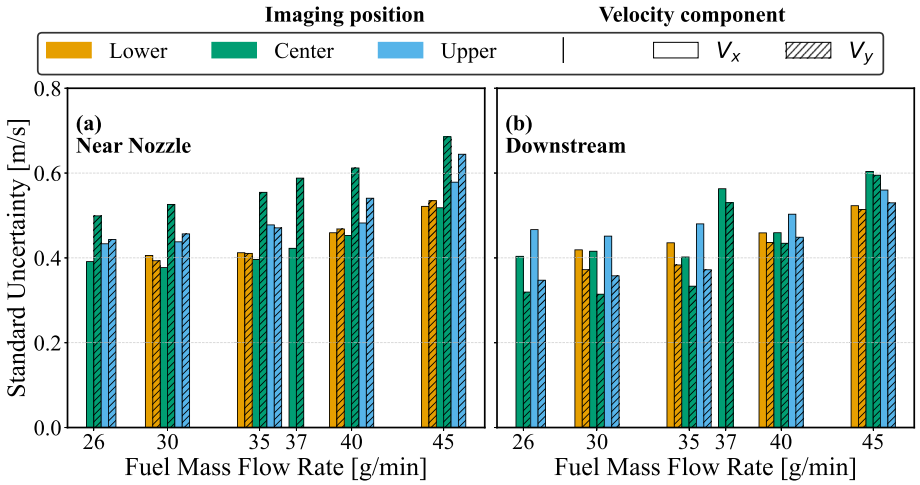

Fig. 12. Average uncertainty estimation for multiple fuel flow rates and imaging positions: (a) near nozzle, and (b) downstream.

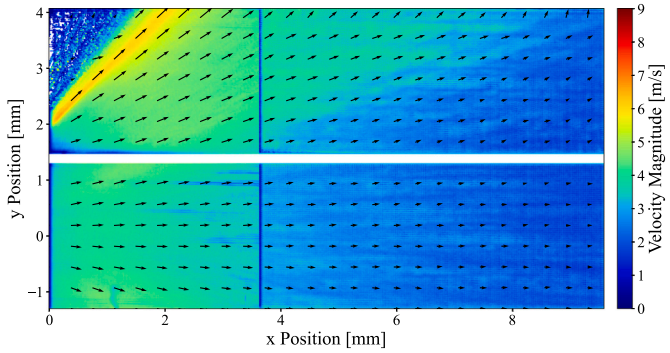

Fig. 13. Averaged velocity contour at a fuel flow rate of 26 g/min.

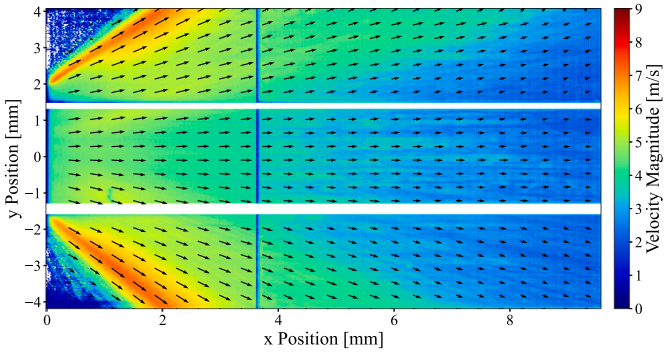

Fig. 14. Averaged velocity contour at a fuel flow rate of 30 g/min.

4. Spray characterization via PC-flow and binarization

4.1. Average flow fields

To analyze the velocity characteristics of the spray under different fuel flow rates, the average velocity fields were computed for three cases: 26 g/min, 30 g/min, and 35 g/min. These cases correspond to different injection conditions, allowing for a comparative analysis of how flow structures evolve with increasing mass flow rates.

The velocity fields were computed within the binarized regions of interest, ensuring that only valid flow data within the segmented spray regions contributed to the average. This approach helped exclude background noise and prevented artifacts from influencing the velocity statistics. The averaging process smooths out transient fluctuations, highlighting dominant flow patterns characteristic of the spray nozzle. The resulting average velocity fields, shown in Figs. 13 to 15, provide insight into the large-scale flow structures and the extent of velocity decay downstream.

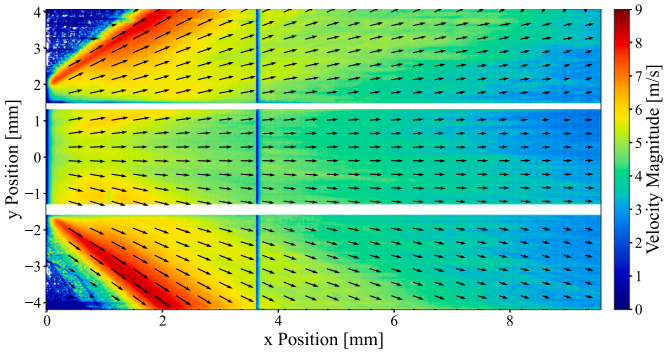

Fig. 15. Averaged velocity contour at a fuel flow rate of 35 g/min.

As expected, higher fuel flow rates exhibited increased velocities due to greater momentum flux at the injector exit. The spray angles were determined from the average binarization field using a Canny edge detection algorithm followed by a Hough transform. The detected spray boundaries for the 35 g/min fuel flow rate condition are illustrated in Fig. 16, and the final spray angle measurements for each fuel mass flow rate tested are listed in Table 5. The spray angles remained relatively constant, varying by less than 2 degrees over the tested fuel mass flow rates.

These results can be used to evaluate the influence of fuel flow rate on spray breakup dynamics and mixing characteristics, serving as a basis for further analysis of turbulence intensity and velocity fluctuations in different regions of the spray. Additionally, the results confirm the physical nature of the spray, accurately capturing the conical structure of the injected fuel as it propagates downstream.

It is essential to interpret these velocity fields within the context of the reacting environment. In non-premixed sprays, it can be a reasonable assumption that the initial spray formation processes occur in relatively low temperature, fuel-rich regions that are physically separate from the high-temperature combustion zones [80]. However, other works have found that the existence of such distinct zones is dependent on the initial droplet sizes [81]. The heat release from combustion influences

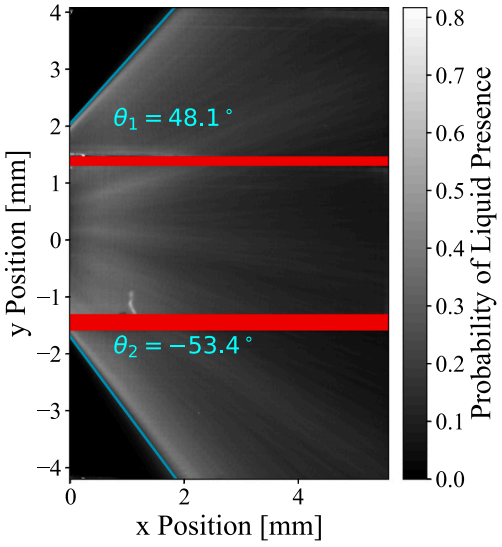

Fig. 16. Spray angle estimation at a fuel flow rate of 35 g/min.

Table 5
Spray angle as a function of fuel flow rate.

Fuel Flow Rate [g/min]	θ_1 [°]	θ_2 [°]	θ_t [°]
26	47.2	–	–
30	47.6	–54.2	102.0
35	48.1	–53.4	101.3
40	48.7	–54.3	103.0
45	47.8	–54.1	102.1

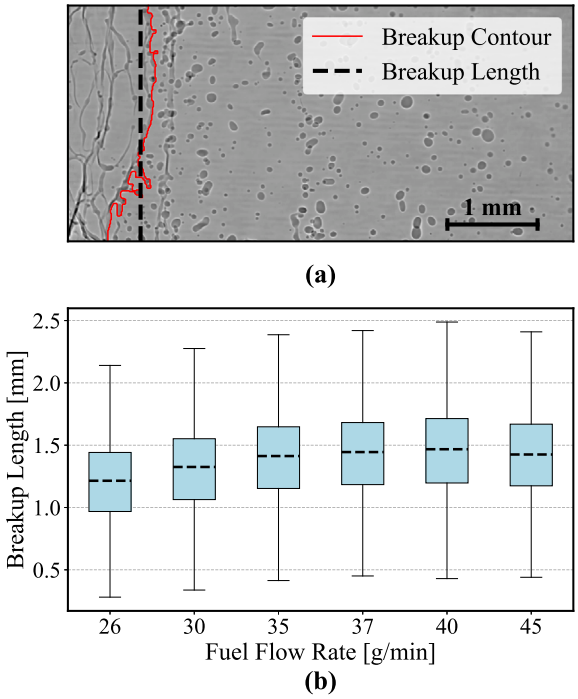

Fig. 17. Breakup length estimation: (a) identification of the breakup point, and (b) box plot of breakup length dispersion (dashed line indicates arithmetic mean, blue box indicates the interquartile range (Q1 to Q3), and vertical whiskers indicate the minimum and maximum values). (For interpretation of the references to colour in this figure legend, the reader is referred to the web version of this article.)

spray dynamics through several coupled mechanisms not present in non-reacting flows [82,83]. These include, but are not limited to (1) increased mean gas velocities, fluctuating velocities, and anisotropy [84], which modifies the aerodynamic forces on the droplets, (2) interfacial instabilities on the liquid sheet, with the specific stabilizing or destabilizing effect dependent on the Weber number of the liquid [85], (3) the reduction of liquid fuel viscosity and surface tension via heat transfer, which typically improves atomization quality [86], and (4) enhanced vaporization rates [87]. Therefore, the measured velocity fields and spray statistics represent the net result of the initial injection momentum and these complex combustion interactions. While the present study does not decouple these effects, it provides a critical dataset of the integrated spray behavior within a realistic combustor environment, which is essential for validating comprehensive spray combustion models.

4.2. Primary breakup analysis

The different roles of the liquid stream's instability and aerodynamic forces allow a distinction to be made between primary and secondary atomization. Primary atomization refers to breakup driven by inertial effects and liquid sheet instability. In contrast, secondary atomization involves the additional influence of aerodynamic forces acting on already fragmented liquid structures [1]. However, the breakup process is inherently transient, and different breakup mechanisms may coexist and compete spatially within the liquid sheet.

To quantify the primary breakup length, the breakup point was identified as presented in Fig. 17(a), demonstrating a method for extracting the primary breakup length of the liquid sheet using binarized images. Here, the breakup length was defined as the furthest downstream position where the sheet remained fully connected across the entire height of the image in the central imaging position. To quantify this location, the contour of the leading edge of the sheet was identified, and its average x-position was computed, serving as a representative metric for the breakup location. Unlike conventional breakup length measurements, this approach inherently captured temporal variations. The breakup length dispersion is displayed in Fig. 17(b), providing a dynamic characterization of the unsteady nature of primary breakup. Most experimental studies on primary breakup rely on independent single-shot images, while only a few investigations provide time-resolved imaging of the breakup process [88,89]. The present approach aimed to bridge this gap by tracking time-dependent variations in the breakup length.

In Fig. 18, the velocity field was analyzed by computing probability density functions (PDFs) at the temporal breakup length of the spray in the central imaging region. All PDFs, including subsequent ones, were computed using a non-parametric Gaussian kernel density estimation with Scott's rule for bandwidth selection. Velocity components were extracted using the binarized image along the temporal contour line, ensuring that only valid liquid fuel-phase velocity values were included. This approach enabled the examination of how the velocity distribution evolves as the sheet disintegrates, providing insights into the underlying dynamics of ligament formation, droplet detachment, and velocity fluctuations during breakup.

The time-averaged primary breakup length (l_b) and its corresponding mean axial velocity derived from Fig. 18(a) for varying fuel flow rates were summarized in Table 6. The breakup length was observed to increase almost linearly with the flow rate, a trend that directly corresponds to the steady increase in the measured arithmetic mean of V_x. The characteristic breakup time, derived as the ratio $\tau_b = l_b/\mathrm{Mean}(V_x)$, remained nearly constant, exhibiting only a slight decrease as the fuel flow rate increased. This near-constant τ_b, especially at higher flow rates, indicated a near-constant primary breakup rate and time of sheet disintegration. Therefore, the observed extension of the breakup length as flow rates increased is principally attributed to the transport of the liquid sheet further downstream during this fixed time period.

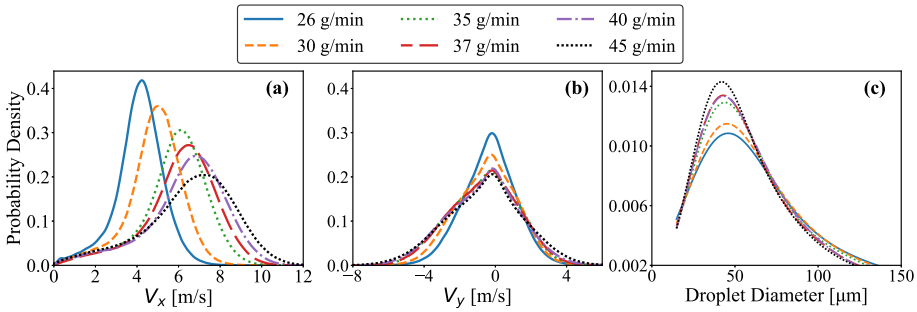

Fig. 18. Probability density function at the breakup location of different fueling rates for (a) V_x, (b) V_y, and (c) droplet diameter.

Table 6
Time-averaged breakup length and characteristic breakup time as a function of fuel flow rate.

Fuel Flow Rate [g/min]	Primary Breakup Length [mm]	Mean V_x [m/s]	τ_b [ms]
26	1.21	4.11	0.29
30	1.33	4.84	0.27
35	1.41	5.77	0.24
37	1.44	6.09	0.24
40	1.47	6.35	0.23
45	1.43	6.51	0.22

Additionally, the droplet diameter PDF was evaluated in Fig. 18(c) at the time-averaged breakup length, as defined in Table 6, using a window size of 15 pixels. The results indicate that higher fuel flow rates lead to smaller average droplet sizes near the breakup point, measured as 92.9, 89.9, 84.2, 83.0, 81.9, and 79.1 μm with respect to increasing flow rates. Together, these analyses illustrate the coupling between velocity variations and droplet size distributions, highlighting key trends in the breakup process.

4.3. Sphericity analysis

A key assumption in phase-Doppler particle anemometry (PDPA) is that liquid droplets are spherical, which is necessary for accurate size and velocity measurements [22,23]. To assess the validity of this assumption, droplet sphericity was computed using the binarization scheme described in Section 3.3. The functional form to determine sphericity was mathematically defined as:

$$\Psi = \frac{4\pi A}{P^2}, \tag{23}$$

where Ψ is the sphericity, A is the area of the binarized shape, and P is the perimeter of the shape, computed from the 2-D projection of the droplet. A sphericity value of 1 corresponds to a perfectly circular cross-section, while lower values indicate deviations from an ideal spherical shape. To incorporate the influence of varying droplet sizes, a mass-averaged sphericity was computed for statistical analysis, assuming constant droplet density (ρ):

$$\overline{\Psi} = \frac{\sum \Psi A}{\sum A}, \tag{24}$$

where $\overline{\Psi}$ represents the weighted sphericity, ensuring that larger droplets have a greater influence on the final estimation. The analysis was conducted only at the central position, incorporating data from both the near-nozzle and downstream regions.

The sphericity criterion utilized was the square of perimeter circularity, often called the Cox circularity. Research by Tripathi et al. found a high linear correlation between 2D perimeter circularity and Wadell's true sphericity [90]. Furthermore, Bagheri et al. demonstrated that using three perpendicular projections can limit the maximum error in 3D shape estimation to less than 10 %. The 2D perimeter circularity exhibits low variance with changes in viewing angle, making it a reliable predictor of 3D shape from any random projection [91]. While a single, complex, irregular shape projected in 2D might result in an inaccurate 3D shape estimation, the statistical distribution of the entire droplet population (>1 M droplets in each imaging area) was large enough to overcome this. Droplet and ligament rotation within turbulent sprays [92,93] ensures random projections. While anisotropic flows may induce alignment, a droplet's shape deforms most significantly along the axial direction. This primary mode of deformation was directly captured by the orthogonal projection imaging. Thus, the 2D projected circularity was justified as a robust proxy for 3D sphericity.

The observation of increase in sphericity as a function of downstream position was measured in a liquid jet [23,94]. Yet, detailed positional sphericity curves are missing from the literature. Fig. 19 presents the variation of sphericity as a function of the x-position (streamwise direction), representing the downstream distance from the nozzle.

Quantification of the primary breakup process is notoriously complicated. Simulation work has demonstrated the messy nature of primary breakup [95,96], indicated by a transition to individual droplets. Using digital off-axis holography, Wang et al. experimentally detected the presence of liquid droplets and ligaments within the primary breakup and perforations of a liquid sheet [97].

The inflection point in the sphericity curve was utilized as another metric to describe the breakup process. This metric captures the underlying physics of sheet instability by tracking the ensemble of individual trackable features in the liquid sheet, compared to tracking the front edge of the liquid sheet. The inflection point mathematically represents where the rate of increase of sphericity is maximal, physically indicating rapid disintegration of the connected columns into individual liquid features. Comparably, experimental breakup length has been quantified from the turning point of void-fraction curves [98] or the decay of a fluorescence signal proportional to the liquid volume fraction [99]. Statistical approaches have identified breakup length as the peak variance of shadowgraph image intensities, signifying maximum sheet instability, while using kurtosis for supplemental analysis of sheet intermittency [100,101].

Although the inflection point positions are comparable with those in Table 6, the results listed in Table 7 indicate a contradictory trend from the previous observations: the streamwise location of the inflection position increases as the fuel flow rate decreases. It is conjectured the leading-edge tracking measures the sheet's breakup process through convective timescale, while the sphericity inflection point measures the sheet's internal instability timescale. At low Reynolds numbers, breakup is governed by slow rim disintegration at the sheet's edge.

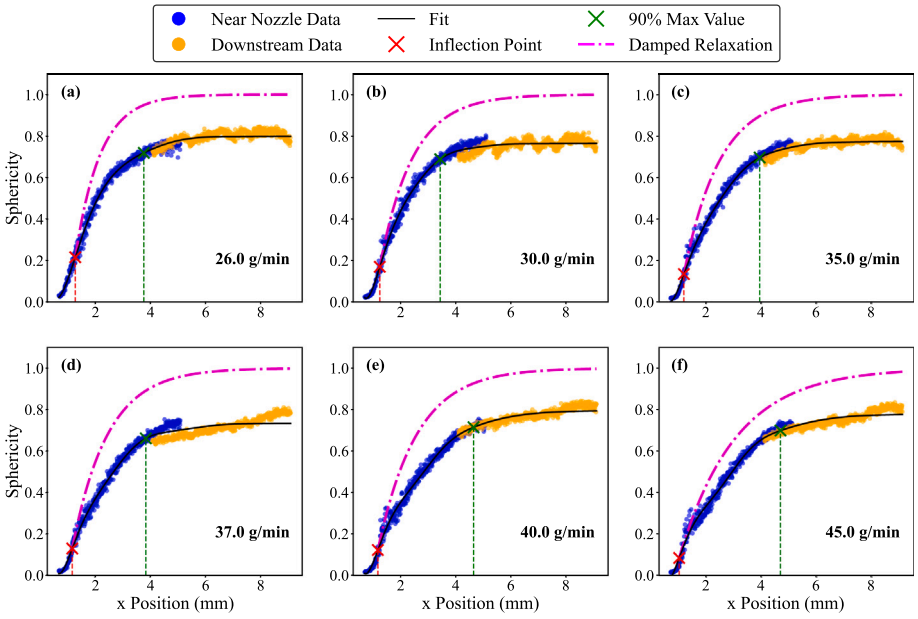

Fig. 19. Sphericity curve along the streamwise direction: (a) 26 g/min, (b) 30 g/min, (c) 35 g/min, d) 37 g/min, e) 40 g/min, and f) 45 g/min.

Table 7
Comparison of experimental and predicted sphericity threshold locations at different fuel flow rates.

Fuel Flow Rate	Inflection Point	Threshold	Sphericity Threshold Location [mm]		
[g/min]	[mm]	Type	10 %	50 %	90 %
26	1.30	Experimental	0.94	1.78	3.78
		Predicted	—	1.71	3.17
30	1.25	Experimental	1.03	1.81	3.44
		Predicted	—	1.86	3.75
35	1.18	Experimental	1.03	2.01	3.93
		Predicted	—	1.89	3.96
37	1.19	Experimental	1.03	2.01	3.85
		Predicted	—	1.90	3.95
40	1.18	Experimental	1.06	2.25	4.65
		Predicted	—	1.97	4.18
45	1.01	Experimental	1.00	2.32	4.68
		Predicted	—	2.22	5.24

However, at higher flow rates, the mechanism transitions to a perforation mode, where instabilities create holes throughout the sheet's interior [102,103]. The sphericity curve measures the rate of transformation from a sheet to individual droplets, a process that occurs closer to the nozzle when perforation dominates.

Beyond this complex breakup region marked by the inflection point, the spray enters a physical regime dominated by droplet relaxation. In this downstream zone, the newly formed oscillating droplets stabilize. This process is governed by two principal forces: surface tension, which acts as a restoring force pulling the droplet into a sphere, and internal liquid viscosity, which acts as a damping force that dissipates the oscillatory energy. This physical behavior is well described by the unforced damped harmonic oscillator model, rooted in Rayleigh-Lamb theory [104,105]. The evolution of a droplet's deformation amplitude (A), as a function of downstream position (x) can be modeled as [106]:

$$A(x) \approx A_0 \cdot e^{-x/(v\tau_d)} \tag{25}$$

where A_0 is the initial deformation amplitude and τ_d is the characteristic damping time. This damping time quantifies the dissipative effect of the liquid's internal viscosity. For any given oscillation mode l, it is a function of the liquid's density (ρ_l), dynamic viscosity (μ_l), and the equilibrium droplet radius (R). In practice, fundamental mode ($l = 2$) is dominant because it is the lowest-energy deformation and most easily excited [107]. The general equation for the damping time is:

$$\tau_{d,l} = \frac{\rho_l R^2}{\mu_l (l-1)(2l+1)}, \text{where } \tau_{d,l=2} = \frac{\rho_l R^2}{5\mu_l}. \tag{26}$$

Using this theory, a predictive model for the evolution of the sphericity envelope, $S(x)$, downstream of the inflection point ($x_{inflection}$) was developed:

$$S(x) \approx 1 - S(x_{inflection}) \cdot e^{-5\mu_l x/(V_x \rho_l R^2)} \tag{27}$$

This physics-based, unforced relaxation model was applied to the experimental data in the region downstream of the inflection point. The characteristic droplet radius R was determined from the average droplet size in a 5-pixel window at the sphericity inflection point, while the axial velocity V_x was taken from the mean values in Table 6. A comparison in Table 7 revealed that the idealized model predicted the relative trends of 50 % and 90 % maximal sphericity well. Yet, the idealized model predicted plateaued sphericity near 1 where the experimental values plateaued around 0.8. This discrepancy suggests effects from aerodynamic forces, which are neglected in the unforced model and act to prolong the non-spherical state of the droplets.

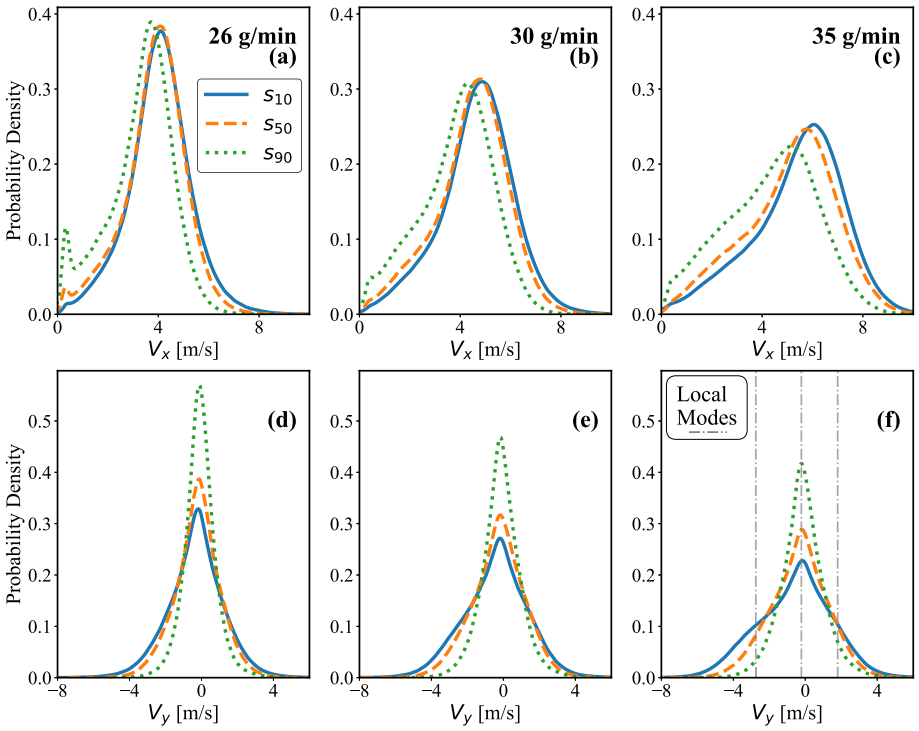

Fig. 20. Velocity components extracted at different sphericity locations.

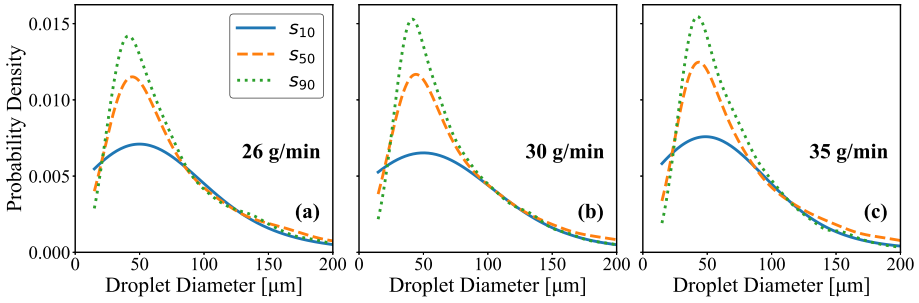

Fig. 21. Probability density function of droplet diameters: (a) 26 g/min, (b) 30 g/min, and (c) 35 g/min.

While the model also omitted secondary breakup, an analysis of the Weber number suggested this was a reasonable simplification. $We < 0.2$ was observed for all cases utilizing absolute droplet velocities. However, a more accurate estimate requires the slip velocity. Simulations at relevant conditions in the ARC-M1 combustor [56] revealed characteristic air velocity of ~ -10 m/s near the central recirculation region where the spray is injected, corresponding to $We < 2$. While significant enough to have caused the observed deviation from the unforced model, this was reasonably below the critical threshold for secondary breakup modes like bag breakup [1]. Future work is needed to quantitatively predict forcing effects.

Fig. 20 illustrates the velocity probability density functions (PDFs) at different x-positions, corresponding to 10 % (s_{10}), 50 % (s_{50}), and 90 % (s_{90}) of the maximum sphericity value from the fit of the sphericity plot. The distribution plots are paired vertically for streamwise (V_x) and transverse (V_y) velocity at three flow rates. The x-positions were determined using a 5-pixel window centered at each selected location, including the center pixel and extending 2 pixels on each side. This windowing approach, in conjunction with the binarized images, ensured that only valid velocity values were extracted for analysis.

Both V_x and V_y exhibited a general decrease in magnitude as the fuel flow rate decreased, reflecting lower injection momentum at lower flow rates. Additionally, a slight asymmetry was observed in V_y, where the distributions tended to be skewed toward negative values, likely due to the influence of gravity on the fuel spray.

At s_{10}, the velocity PDFs reveal a slight trimodal distribution for V_y, suggesting increased transverse velocity fluctuations in the high-shear breakup region. This behavior indicates a more chaotic and irregular breakup process, likely influenced by small-scale instabilities. At the downstream s_{50} and s_{90} locations, the trimodal distribution progressively smooths out, suggesting that downstream transport leads to a more developed velocity field.

Fig. 21 presents the probability density distribution of the droplet equivalent diameter, once again categorized by x-positions at 10 %, 50 %, and 90 % of the maximum sphericity value. The results indicate that droplet size generally decreased as the fuel flow rate increased, though this effect remained relatively small over the tested flow rates. This trend aligned with expectations, as higher injection velocities lead to better atomization and smaller droplet sizes.

5. Conclusions

This study presented a novel approach for improving optical flow estimations and subsequently analyzing fuel spray breakup using

high-speed X-ray phase contrast imaging. Through the implementation of a CNN-based optical flow model and a binarization technique, this work successfully extracted velocity vectors across the region of interest, along with quantitative measurements of droplet size, sphericity, and breakup length. These results provided a comprehensive characterization of the spray breakup process, demonstrating the effectiveness of the proposed methodology.

Built upon the UPFlow model, an attention mechanism and improved upsampling approach were introduced to the proposed PC-Flow model for better capturing the features of liquid-gas boundaries. PC-Flow yielded fewer parameters and shorter training times while showing better accuracies compared to the reference UPFlow model in many error metrics. Moreover, PC-Flow demonstrated increased performance in suppressing error propagation across multiple time steps, offering higher accuracy and reliability of the predicted velocity estimations.

Subsequently, the proposed scheme was applied to the X-ray PCI images to characterize the spray atomization combined with the binarization technique. As a result, time-resolved flow quantity distributions, including particle velocities, size, breakup length, and sphericity were obtained. The results demonstrated that the primary breakup length, defined as the furthest downstream position where the sheet remains fully connected, increased with increasing fuel flow rate. Moreover, to evaluate the validity of the perfectly spherical droplet assumption in the secondary breakup region, circularity was analyzed for liquid structures extracted from binarized images. The sphericity analysis as a function of downstream distance revealed a transition in the breakup process, with an inflection point in the data indicating the shift to separated liquid structures. This estimation revealed two competing effects from the elevated velocities, one from the transport of the liquid and the other from the accelerated sheet disintegration and perforation in the upstream region. The probability density functions (PDFs) of velocity distributions at specific sphericity thresholds further highlighted the evolving spray dynamics, showing that both streamwise and transverse velocity components exhibit characteristic shifts in response to fuel flow rate.

This work offers a uniquely time-resolved perspective on primary breakup, contrasting with traditional single-shot imaging techniques. The ability to track the evolution of the breakup length over time provides deeper insights into the transient nature of liquid sheet disintegration, highlighting the interplay between sheet instability, aerodynamic forces, and fuel flow rate in governing atomization behavior. Therefore, the methodologies developed in this study can provide a foundation for more detailed investigations into spray morphology and fuel-air mixing in advanced combustion systems, offering time-resolved critical parameters of spray including velocity, size distribution, breakup length, and sphericity in a unified framework. Accordingly, future work will focus on exploring the impact of fuel properties on breakup characteristics as well as spray-combustion interaction in combusting vs. non-combusting sprays.

CRediT authorship contribution statement

Casey J. O'Brien: Writing – review & editing, Writing – original draft, Visualization, Validation, Software, Methodology, Investigation, Formal analysis, Conceptualization. **Kyungrae Kang:** Writing – review & editing, Writing – original draft, Conceptualization. **Eric J. Wood:** Writing – review & editing, Investigation, Data curation. **Joshua Yoon:** Writing – review & editing. **Eric K. Mayhew:** Project administration, Data curation. **Alan Kastengren:** Supervision, Resources. **Chol-Bum M. Kweon:** Resources. **Tonghun Lee:** Project administration, Funding acquisition.

Declaration of competing interest

The authors declare that they have no known competing financial interests or personal relationships that could have appeared to influence the work reported in this paper.

Acknowledgments

This research was sponsored by the DEVCOM Army Research Laboratory and was accomplished under Cooperative Agreement Number W911NF-24–2-0031. The views and conclusions contained in this document are those of the authors and should not be interpreted as representing the official policies, either expressed or implied, of the Army Research Laboratory or the US Government. The US Government is authorized to reproduce and distribute reprints for Government purposes notwithstanding any copyright notation herein.

This research was funded by the U.S. Federal Aviation Administration Office of Environment and Energy through ASCENT, the FAA Center of Excellence for Alternative Jet Fuels and the Environment, project 65 b Rapid Jet Fuel Prescreening through FAA Award Number DOT FAA 13-C-AJFE-UI 051 under the supervision of Ana Gabrielian and Sydney Van De Meulebroecke. Any opinions, findings, conclusions, or recommendations expressed in this material are those of the authors and do not necessarily reflect the views of the FAA.

Use of the Advanced Photon Source was supported by the U. S. Department of Energy, Office of Science, Office of Basic Energy Sciences, under Contract No. DE-AC02-06CH11357.

Data availability

Data will be made available on request. Code will be made publicly available on GitHub upon publication of the article.

References

[1] Lefebvre AH, McDonell VG. Atomization and sprays. 2nd ed. CRC Press; 2017. https://doi.org/10.1201/9781315120911
[2] Hiroyasu H. Spray breakup mechanism from the hole-type nozzle and ITS applications. Atomization Sprays 2000;10(3–5). https://doi.org/10.1615/AtomizSpr.v10.i3-5.130
[3] Rezaei S, Vashahi F, Ryu G, Lee J. On the correlation of the primary breakup length with fuel temperature in pressure swirl nozzle. Fuel 2019;258:116094. https://doi.org/10.1016/j.fuel.2019.116094
[4] Lešnik L, Kegl B, Bombek G, Hočevar M, Biluš I. The influence of in-nozzle cavitation on flow characteristics and spray break-up. Fuel 2018;222:550–60. https://doi.org/10.1016/j.fuel.2018.02.144
[5] Warncke K, Gepperth S, Sauer B, Sadiki A, Janicka J, Koch R, Bauer H-J. Experimental and numerical investigation of the primary breakup of an air-blasted liquid sheet. Int J Multiph Flow 2017;91:208–24. https://doi.org/10.1016/j.ijmultiphaseflow.2016.12.010
[6] Gorokhovski M, Herrmann M. Modeling primary atomization. Annu Rev Fluid Mech 2008;40(1):343–66. https://doi.org/10.1146/annurev.fluid.40.111406.102200
[7] Lasheras JC, Hopfinger EJ. Liquid jet instability and atomization in a coaxial gas stream. Annu Rev Fluid Mech 2000;32(1):275–308. https://doi.org/10.1146/annurev.fluid.32.1.275
[8] Shinjo J, Umemura A. Surface instability and primary atomization characteristics of straight liquid jet sprays. Int J Multiphase Flow 2011;37(10):1294–304. https://doi.org/10.1016/j.ijmultiphaseflow.2011.08.002
[9] Xu Z, Wang T, Che Z. Droplet breakup in airflow with strong shear effect. J Fluid Mech 2022;941:A54. https://doi.org/10.1017/jfm.2022.326
[10] Durdina L, Jedelsky J, Jicha M. Investigation and comparison of spray characteristics of pressure-swirl atomizers for a small-sized aircraft turbine engine. Int J Heat Mass Transf 2014;78:892–900. https://doi.org/10.1016/j.ijheatmasstransfer.2014.07.066
[11] Zhang T, Dong B, Chen X, Qiu Z, Jiang R, Li W. Spray characteristics of pressure-swirl nozzles at different nozzle diameters. Appl Therm Eng 2017;121:984–91. https://doi.org/10.1016/j.applthermaleng.2017.04.089
[12] Kirar PK, Kumar N, Sahu KC. Dynamics of jet breakup and the resultant drop size distribution-effect of nozzle size and impingement velocity. Phys Fluids 2024;36(10). https://doi.org/10.1063/5.0225452
[13] Chen SK, Lefebvre AH, Rollbuhler J. Factors influencing the circumferential liquid distribution from pressure-swirl atomizers. J Eng Gas Turbines Power 1993;115(3):447–52. https://doi.org/10.1115/1.2906729
[14] Santolaya JL, Aísa LA, Calvo E, García I, Cerecedo LM. Experimental study of near-field flow structure in hollow cone pressure swirl sprays. J Propuls Power 2007;23(2):382–9. https://doi.org/10.2514/1.20713
[15] Shao D, Al Obaid S, Alharbi SA, Maroušek J, Sekar M, Gunasekar P, Chi NTL, Brindhadevi K, Wang J, Jiang D. Prediction of the fuel spray characteristics in the combustion chamber with methane and TiO2 nanoparticles VIA numerical modelling. Fuel 2022;326:124820. https://doi.org/10.1016/j.fuel.2022.124820
[16] Woo S, Lee J, Lee I, Kim S, Han Y, Yoon Y. Analyzing combustion efficiency according to spray characteristics of gas-centered swirl-coaxial injector. Aerospace 2023;10(3):274. https://doi.org/10.3390/aerospace10030274

[17] Settles GS. Schlieren and Shadowgraph techniques: visualizing phenomena in transparent media. Springer Science & Business Media; 2001. https://doi.org/10.1007/978-3-642-56640-0

[18] Castrejón-García R, Castrejón-Pita JR, Martin GD, Hutchings IM. The Shadowgraph imaging technique and ITS modern application to fluid jets and drops. Rev Mex Fis 2011;57(3):266–75.

[19] Coghe A, Cossali GE. Quantitative optical techniques for dense sprays investigation: a survey. Opt Lasers Eng 2012;50(1):46–56. https://doi.org/10.1016/j.optlaseng.2011.07.017

[20] Cao Z-M, Nishino K, Mizuno S, Torii K. Piv measurement of internal structure of diesel fuel spray. Experiments In Fluids 2000;29(Suppl 1):211–9. https://doi.org/10.1007/s003480070023

[21] Rottenkolber G, Gindele J, Raposo J, Dullenkopf K, Hentschel W, Wittig S, Spicher U, Merzkirch W. Spray analysis of a gasoline direct injector by means of two-phase piv. Exp Fluids 2002;32:710–21. https://doi.org/10.1007/s00348-002-0441-8

[22] Bachalo WD, Houser MJ. Phase/doppler spray analyzer for simultaneous measurements of drop size and velocity distributions. Opt Eng 1984;23(5):583–90. https://doi.org/10.1117/12.7973341

[23] Malot H, Blaisot J-B. Droplet size distribution and sphericity measurements of low-density sprays through image analysis. Part Part Syst Charact 2000;17(4):146–58. https://doi.org/10.1002/1521-4117(200012)17:4

[24] Kastengren A, Powell CF. Synchrotron x-ray techniques for fluid dynamics. Exp Fluids Feb 2014;55(3). https://doi.org/10.1007/s00348-014-1686-8

[25] Alfarano A, Maiano L, Papa L, Amerini I. Estimating optical flow: a comprehensive review of the state of the art. Comput Vis Image Underst 2024:104160. https://doi.org/10.1016/j.cviu.2024.104160

[26] Dosovitskiy A, Fischer P, Ilg E, Häusser P, Hazirbas C, Golkov V, Smagt PVD, Cremers D, Brox T. Flownet: learning optical flow with convolutional networks, In: 2015 IEEE International Conference on Computer vision (ICCV); 2015. p. 2758–66. https://doi.org/10.1109/ICCV.2015.316

[27] Ilg E, Mayer N, Saikia T, Keuper M, Dosovitskiy A, Brox T. Flownet 2.0: evolution of optical flow estimation with deep networks, In: 2017 IEEE conference on Computer vision and pattern recognition (CVPR); 2017. p. 1647–55. https://doi.org/10.1109/CVPR.2017.179

[28] Sun D, Yang X, Liu M-Y, Kautz J. Pwc-Net: CNNS for optical flow using pyramid, warping, and cost volume, In: 2018 IEEE/CVF conference on Computer vision and pattern recognition; 2018. p. 8934–43. https://doi.org/10.1109/CVPR.2018.00931

[29] Teed Z, Deng J. Raft: recurrent all-pairs field transforms for optical flow, In: Computer vision–ECCV 2020: 16th European Conference, Glasgow, UK, August 23–28, 2020, proceedings, part II 16; Springer; 2020. p. 402–19. https://doi.org/10.1007/978-3-030-58536-5_24

[30] Huang Z, Shi X, Zhang C, Wang Q, Cheung KC, Qin H, Dai J, Li H. Flowformer: a transformer architecture for optical flow, In: European Conference on Computer vision; Springer; 2022. p. 668–85. https://doi.org/10.1007/978-3-031-19790-1_40

[31] Ren Z, Yan J, Ni B, Liu B, Yang X, Zha H. Unsupervised deep learning for optical flow estimation, In: Proceedings of the AAAI Conference on Artificial Intelligence, vol. 31. 2017. https://doi.org/10.1609/aaai.v31i1.10723

[32] Wang Y, Yang Y, Yang Z, Zhao L, Wang P, Xu W. Occlusion aware unsupervised learning of optical flow, In: 2018 IEEE/CVF conference on Computer vision and pattern recognition; 2018. p. 4884–93. https://doi.org/10.1109/CVPR.2018.00513

[33] Liu P, King I, Lyu MR, Xu J. Ddflow: learning optical flow with unlabeled data distillation, In: Proceedings of the AAAI Conference on Artificial Intelligence, vol. 33. 2019. p. 8770–7. https://doi.org/10.1609/aaai.v33i01.33018770

[34] Jonschkowski R, Stone A, Barron JT, Gordon A, Konolige K, Angelova A. What matters in unsupervised optical flow, In: Computer vision–ECCV 2020: 16th European Conference, Glasgow, UK, August 23–28, 2020, proceedings, part II 16; Springer; 2020. p. 557–72. https://doi.org/10.1007/978-3-030-58536-5_33

[35] Luo K, Wang C, Liu S, Fan H, Wang J, Sun J. Upflow: upsampling pyramid for unsupervised optical flow learning, In: 2021 IEEE/CVF conference on Computer vision and pattern recognition (CVPR); 2021. p. 1045–54. https://doi.org/10.1109/CVPR46437.2021.00110

[36] Xiang X, Abdein R, Lv N, El Saddik A. Invflow: involution and multi-scale interaction for unsupervised learning of optical flow. Pattern Recognit 2024;145:109918. https://doi.org/10.1016/j.patcog.2023.109918

[37] Ranjan A, Black MJ. Optical flow estimation using a spatial pyramid network, In: 2017 IEEE conference on Computer vision and pattern recognition (CVPR); 2017. p. 2720–9. https://doi.org/10.1109/CVPR.2017.291

[38] Ahmadi A, Patras I. Unsupervised convolutional neural networks for motion estimation, In: 2016 IEEE International Conference on image Processing (ICIP); IEEE; 2016. p. 1629–33. https://doi.org/10.1109/ICIP.2016.7532634

[39] Meister S, Hur J, Roth S. Unflow: unsupervised learning of optical flow with a bidirectional census loss, In: Proceedings of the AAAI Conference on Artificial Intelligence, vol. 32. 2018. https://doi.org/10.1609/aaai.v32i1.12276

[40] Liu P, Lyu M, King I, Xu J. Selflow: Self-supervised learning of optical flow, In: 2019 IEEE/CVF conference on Computer vision and pattern recognition (CVPR); 2019. p. 4566–75. https://doi.org/10.1109/CVPR.2019.00470

[41] Ren Z, Luo W, Yan J, Liao W, Yang X, Yuille A, Zha H. Stflow: self-taught optical flow estimation using pseudo labels. IEEE Trans Image Process 2020;29:9113–24. https://doi.org/10.1109/TIP.2020.3024015

[42] Janai J, Güney F, Ranjan A, Black M, Geiger A. Unsupervised learning of multi-frame optical flow with occlusions, In: Ferrari V, Hebert M, Sminchisescu C, Weiss Y, editors. Computer vision – ECCV 2018; Cham: Springer International Publishing; 2018. p. 713–31. https://doi.org/10.1007/978-3-030-01270-0_42

[43] Zhong Y, Ji P, Wang J, Dai Y, Li H. Unsupervised deep epipolar flow for stationary or dynamic scenes, In: 2019 IEEE/CVF conference on Computer vision and pattern recognition (CVPR); 2019. p. 12087–96. https://doi.org/10.1109/CVPR.2019.01237

[44] Ranjan A, Jampani V, Balles L, Kim K, Sun D, Wulff J, Black MJ. Competitive collaboration: joint unsupervised learning of depth, camera motion, optical flow and motion segmentation, In: 2019 IEEE/CVF conference on Computer vision and pattern recognition (CVPR); 2019. p. 12232–41. https://doi.org/10.1109/CVPR.2019.01252

[45] Yin Z, Shi J. Geonet: unsupervised learning of dense depth, optical flow and camera pose, In: 2018 IEEE/CVF conference on Computer vision and pattern recognition; 2018. p. 1983–92. https://doi.org/10.1109/CVPR.2018.00212

[46] Zou Y, Luo Z, Huang J-B. Df-net: unsupervised joint learning of depth and flow using cross-task consistency, In: Ferrari V, Hebert M, Sminchisescu C, Weiss Y, editors. Computer vision – ECCV 2018; Cham: Springer International Publishing; 2018. p. 38–55. https://doi.org/10.1007/978-3-030-01228-1_3

[47] Liu L, Zhai G, Ye W, Liu Y. Unsupervised learning of scene flow estimation fusing with local rigidity, In: IJCAI; 2019. p. 876–82. https://doi.org/10.24963/ijcai.2019/123

[48] Hwang J, Lee P, Mun S, Karathanassis IK, Koukouvinis P, Pickett LM, Gavaises M. Machine-learning enabled prediction of 3d spray under engine combustion network spray g conditions. Fuel 2021;293:120444. https://doi.org/10.1016/j.fuel.2021.120444

[49] Hasti VR, Shin D. Denoising and fuel spray droplet detection from light-scattered images using deep learning. Energy And AI 2022;7:100130. https://doi.org/10.1016/j.egyai.2021.100130

[50] Kumar MS, Hogan CJ, Fredericks SA, Hong J. Visualization and characterization of agricultural sprays using machine learning based digital inline holography. Comput Electron Agric 2024;216:108486. https://doi.org/10.1016/j.compag.2023.108486

[51] Zhang Z, Wang J, Zhao H, Mu Z, Chen L. Applicability of deep learning optical flow estimation for piv methods. Flow Meas Instrum 2023;93:102398. https://doi.org/10.1016/j.flowmeasinst.2023.102398

[52] Lagemann C, Lagemann K, Mukherjee S, Schröder W. Challenges of deep unsupervised optical flow estimation for particle-image velocimetry data. Exp Fluids 2024;65(3):30. https://doi.org/10.1007/s00348-024-03768-2

[53] Choi D, Kim H, Park H. Bubble velocimetry using the conventional and Cnn-based optical flow algorithms. Scientific Reports 2022;12(1):11879. https://doi.org/10.1038/s41598-022-16145-y

[54] Zhang D, Yang Z. Deep learning-based optical flow analysis of two-dimensional Rayleigh scattering imaging of high-speed flows. J Vis 2024;27(3):323–31. https://doi.org/10.1007/s12650-024-00978-y

[55] Wood EJ, Mayhew E, Motily A, Temme J, Kweon C-B, Lee T. Lean blowout dependence on fuel properties and combustion conditions in the arc-m1 single-cup swirl combustor. AIAA scit. 2021 Forum 2021:0364. https://doi.org/10.2514/6.2021-0652

[56] Dasgupta D, Som S, Wood E, Lee T, Mayhew E, Temme J, Kweon C-B. Computational Fluid dynamics modeling of fuel properties impact on lean blowout in the arc-M1 combustor. Turbo Expo Power Land Sea Air 2022;85994:V03AT04A010. https://doi.org/10.1115/GT2022-79347

[57] Wood EJ, Motily A, Trotter CJ, Lee T, Mayhew E, Coburn VD, Temme J, Kweon C-B. Fuel spray and operating condition impact on ignition performance in the arc-M1 combustor. AIAA scit Forum 2022:0364. https://doi.org/10.2514/6.2022-0364

[58] Mayhew E, Wood E, McGann B, Mitsingas C, Oldani A, Rajasegar R, Temme J, Kweon C-B, Matusik KE, Kastengren AL, Lee T. High-speed phase contrast imaging of spray breakup of jet fuels under combusting conditions. Atom Sprays 2021;31(1):31–46. https://doi.org/10.1615/AtomizSpr.2020034440

[59] Wood EJ. Characterization of compact gas turbine combustors for alternative fuel integration, [Ph.D. thesis], University of Illinois at Urbana-Champaign; 2023.

[60] Quan Y, Chen M, Pang T, Ji H. Self2self with dropout: learning self-supervised denoising from single image, In: 2020 IEEE/CVF conference on Computer vision and pattern recognition (CVPR); 2020. p. 1887–95. https://doi.org/10.1109/CVPR42600.2020.00196

[61] Oh J-H, Wood E, Mayhew E, Kastengren A, Lee T. Sequence2self: self-supervised image sequence denoising of pixel-level spray breakup morphology. Eng Appl Art Int 2023;126:106957. https://doi.org/10.1016/j.engappai.2023.106957

[62] Wang Z, Simoncelli EP, Bovik AC. Multiscale structural similarity for image quality assessment, In: The thrity-seventh Asilomar Conference on Signals, Systems & Computers, 2003, vol. 2. 2003. p. 1398–402. https://doi.org/10.1109/ACSSC.2003.1292216

[63] Wang Z, Bovik AC. A universal image quality index. IEEE Signal Process Lett 2002;9(3):81–4. https://doi.org/10.1109/97.995823

[64] Zhang R, Isola P, Efros AA, Shechtman E, Wang O. The unreasonable effectiveness of deep features as a perceptual metric, In: 2018 IEEE/CVF conference on Computer vision and pattern recognition; 2018. p. 586–95. https://doi.org/10.1109/CVPR.2018.00068

[65] Geiger A, Lenz P, Urtasun R. Are we ready for autonomous driving? the Kitti vision benchmark suite, In: 2012 IEEE conference on Computer vision and pattern recognition; 2012. p. 3354–61. https://doi.org/10.1109/CVPR.2012.6248074

[66] Menze M, Geiger A. Object scene flow for autonomous vehicles, In: 2015 IEEE conference on Computer vision and pattern recognition (CVPR); 2015. p. 3061–70. https://doi.org/10.1109/CVPR.2015.7298925

[67] Vaswani A. Attention is all you need. Adv Neural Inf Process Syst 2017.

[68] Serra J, Vincent L. An overview of morphological filtering. Circ Syst Signal Process 1992;11(1):47–108. https://doi.org/10.1007/BF01189221

[69] Bhutada S, Yashwanth N, Dheeraj P, Shekar K. Opening and closing in morphological image processing. World J Adv Res Rev 2022;14(3):687–95. https://doi.org/10.30574/wjarr.2022.14.3.0576

[70] Said KAM, Jambek AB, Sulaiman N. A study of image processing using morphological opening and closing processes. Int J Control Theory Appl 2016;9(31):15–21.

[71] Sun D, Roth S, Lewis JP, Black MJ. Learning optical flow, In: Forsyth D, Torr P, Zisserman A, editors. Computer vision – ECCV 2008; Berlin, Heidelberg: Springer Berlin Heidelberg; 2008. p. 83–97. https://doi.org/10.1007/978-3-540-88690-7_7

[72] Xiang X, Zhai M, Zhang R, Qiao Y, El Saddik A. Deep optical flow supervised learning with prior assumptions. IEEE Access 2018;6:43222–32. https://doi.org/10.1109/ACCESS.2018.2863233

[73] Brox T, Bruhn A, Papenberg N, Weickert J. High accuracy optical flow estimation based on a theory for warping, In: European Conference on Computer vision; Springer; 2004. p. 25–36. https://doi.org/10.1007/978-3-540-24673-2_3

[74] Horn BKP, Schunck BG. Determining optical flow. Artif Intell 1981;17(1–3):185–203. https://doi.org/10.1016/0004-3702(81)90024-2

[75] Lucas BD, Kanade T. An iterative image registration technique with an application to stereo vision, In: IJCAI'81: 7th International Joint Conference on Artificial Intelligence, vol. 2. 1981. p. 674–9.

[76] Sun D, Roth S, Black MJ. A quantitative analysis of current practices in optical flow estimation and the principles behind them. Int J Comput Vis 2014;106(2):115–37. https://doi.org/10.1007/s11263-013-0644-x

[77] Fleet D, Weiss Y. Optical flow estimation. In: Handbook of mathematical models in computer vision. Springer; 2006. pp. 237–57. https://doi.org/10.1007/0-387-28831-7_15

[78] Simoncelli EP, Adelson EH, Heeger DJ. Probability distributions of optical flow, In: Proceedings. 1991 IEEE Computer Society Conference on Computer vision and pattern recognition; 1991. p. 310–5. https://doi.org/10.1109/CVPR.1991.139707

[79] Ilg E, Çiçek Ö, Galesso S, Klein A, Makansi O, Hutter F, Brox T. Uncertainty estimates and multi-hypotheses networks for optical flow, In: Ferrari V, Hebert M, Sminchisescu C, Weiss Y, editors. Computer vision – ECCV 2018; Cham: Springer International Publishing; 2018. p. 677–93. https://doi.org/10.1007/978-3-030-01234-2_40

[80] Faeth GM. Spray combustion phenomena, In: Symposium (international) on combustion, vol. 26. Elsevier; 1996. p. 1593–612. https://doi.org/10.1016/S0082-0784(96)80383-3

[81] Nakamura M, Akamatsu F, Kurose R, Katsuki M. Combustion mechanism of liquid fuel spray in a gaseous flame. Phys Fluids 2005;17(12). https://doi.org/10.1063/1.2140294

[82] Yaozhi ZHOU, Zun CAI, Qinglian LI, Chenyang LI, Mingbo SUN, Shaotian GONG. Characteristics of penetration and distribution of a liquid jet in a divergent cavity-based combustor. Chin J Aeronaut 2023;36(12):139–50. https://doi.org/10.1016/j.cja.2023.03.006

[83] Cai Z, Zhou Y, Li F, Yang X, Chen Z, Wang T, Sun M. Investigation on spray characteristics and mixing mechanism of a backpressure-driven liquid jet in supersonic flows. Phys Fluids 2024;36(12). https://doi.org/10.1063/5.0239529

[84] McDonell VG, Samuelsen S. Gas and drop behavior in reacting and non-reacting air-blast atomizer sprays. J Propuls Power 1991;7(5):684–91. https://doi.org/10.2514/3.23380

[85] Jia B-Q, Yang L-J, Xie L, Fu Q-F, Cui X. Linear stability of confined swirling annular liquid layers in the presence of gas velocity oscillations with heat and MASS transfer. Int J Heat Mass Transf 2019;138:117–25. https://doi.org/10.1016/j.ijheatmasstransfer.2019.04.035

[86] Lefebvre AH, Ballal DR. Gas turbine combustion: alternative fuels and emissions. CRC Press; 2010. https://doi.org/10.1201/9781420086058

[87] Kitano T, Nishio J, Kurose R, Komori S. Evaporation and combustion of multicomponent fuel droplets. Fuel 2014;136:219–25. https://doi.org/10.1016/j.fuel.2014.07.045

[88] Rezayat S, Farshchi M, Berrocal E. High-speed imaging database of water jet disintegration Part II: Temporal Analysis of the Primary Breakup. Int J Multiphase Flow 2021;145:103807. https://doi.org/10.1016/j.ijmultiphaseflow.2021.103807

[89] Kumar A, Sahu S. Liquid jet breakup unsteadiness in a coaxial air-blast atomizer. Int J Spray Combust Dyn 2018;10(3):211–30. https://doi.org/10.1177/1756827718760905

[90] Tripathi P, Lee SJ, Lee CH, Shin M. Towards 3d shape estimation from 2d particle images: a state-of-the-art review and demonstration. KONA Powder And Particle Journal 2025;42:37–56. https://doi.org/10.14356/kona.2025017

[91] Bagheri GH, Bonadonna C, Manzella I, Vonlanthen P. On the characterization of size and shape of irregular particles. Powder Technol 2015;270:141–53. https://doi.org/10.1016/j.powtec.2014.10.015

[92] Roa I, Renoult M-C, Dumouchel C, Brändle de Motta JC. Droplet oscillations in a turbulent flow. Frontiers In Physics 2023;11:1173521. https://doi.org/10.3389/fphy.2023.1173521

[93] Deberne C, Chéron V, Poux A, de Motta JCB. Breakup prediction of oscillating droplets under turbulent flow. Int J Multiphase Flow 2024;173:104731. https://doi.org/10.1016/j.ijmultiphaseflow.2024.104731

[94] Blaisot JB, Yon J. Droplet size and morphology characterization for dense sprays by image processing: application to the diesel spray. Experiments In Fluids 2005;39(6):977–94. https://doi.org/10.1007/s00348-005-0026-4

[95] Lebas R, Menard T, Beau P-A, Berlemont A, Demoulin F-X. Numerical simulation of primary break-up and atomization: DNS and modelling study. Int J Multiphase Flow 2009;35(3):247–60. https://doi.org/10.1016/j.ijmultiphaseflow.2008.11.005

[96] Shinjo J, Umemura A. Simulation of liquid jet primary breakup: dynamics of ligament and droplet formation. Int J Multiphase Flow 2010;36(7):513–32. https://doi.org/10.1016/j.ijmultiphaseflow.2010.03.008

[97] Wang L, Wu Y, Zhang L, Wang D, Yin J, Lin W, Song G, Wu X, Huang Y. Conical liquid sheet morphology and 3d droplet distribution of aviation kerosene pressure-swirl spray with digital off-axis holography. Opt Lett 2023;162:109250. https://doi.org/10.1016/j.optlastec.2023.109250

[98] Davy MH, Loustalan PW. On the sheet breakup of direct-injection gasoline pressure-swirl atomizer sprays. Atomization And Sprays 2007;17(6). https://doi.org/10.1615/AtomizSpr.v17.i6.20

[99] Stepowski D, Werquin O. Measurement of the liquid volume fraction and ITS statistical distribution in the near development field of a spray. Atomization And Sprays 2004;14(3). https://doi.org/10.1615/AtomizSpr.v14.i3.30

[100] Kannaiyan K, Sadr R. The effects of alumina nanoparticles as fuel additives on the spray characteristics of gas-to-liquid jet fuels. Exp Therm Fluid Sci 2017;87:93–103. https://doi.org/10.1016/j.expthermflusci.2017.04.027

[101] Kannaiyan K, Sadr R. Comparison of near-nozzle spray performance of gas-to-liquid and jet a-1 fuels using shadowgraph and phase Doppler anemometry. J Energy Resour Technol 2018;140(7):072009. https://doi.org/10.1115/1.4039271

[102] Liu Y, Zhang H, Li Y, Zhao Z. Numerical investigation on the hole characteristics and perforation mechanism of conical liquid sheet. Therm Sci Eng Prog 2022;29:101225. https://doi.org/10.1016/j.tsep.2022.101225

[103] Liu Y, Liu G, Xu H, Chen L, Qin S, Chao Y, Zhang H. Research on breakup length and atomization characteristics of the swirl liquid sheet in perforation disintegration mode. Phys Fluids 2023;35(12). https://doi.org/10.1063/5.0184316

[104] Rayleigh L. On the capillary phenomena of jets. Proc R Soc Lond 1879:71–97.

[105] Lamb H. Hydrodynamics. University Press; 1924.

[106] Becker E, Hiller WJ, Kowalewski TA. Experimental and theoretical investigation of large-amplitude oscillations of liquid droplets. J Fluid Mech 1991;231:189–210. https://doi.org/10.1017/S0022112091003361

[107] Brenn G, Plohl G. The oscillating drop method for measuring the deformation retardation time of viscoelastic liquids. J Non-Newtonian Fluid Mech 2015;223:88–97. https://doi.org/10.1016/j.jnnfm.2015.05.011